**51st AIAA/ASME/ASCE/AHS/ASC Structures, Structural Dynamics, and Materials Conference
 18th**
12 - 15 April 2010, Orlando, Florida

AIAA 2010-2888

Aeroelastic Analysis of a MAV-Scale Cycloidal Rotor

Moble Benedict [*] and Inderjit Chopra [†]

Alfred Gessow Rotorcraft Center, University of Maryland, College Park, MD, 20742

Mattia Mattaboni [‡] and Pierangelo Masarati [§]

Politecnico di Milano, Department of Aerospace Engineering, 20156 Milano, Italy

Abstract

This paper describes the aeroelastic model to predict the blade loads and the average thrust of a micro air vehicle (MAV) scale cycloidal rotor. The analysis was performed using two approaches, one using a non-linear FEM analysis for moderately flexible blades and second using a multibody based large-deformation analysis (especially applicable for extremely flexible blades). An unsteady aerodynamic model is included in the analysis with two different inflow models, uniform inflow and a double-multiple streamtube inflow model. For the cycloidal rotors using moderately flexible blades, the aeroelastic analysis was able to predict the average thrust with sufficient accuracy over a wide range of rotational speeds, pitching amplitudes and number of blades. However, for the extremely flexible blades, the thrust was underpredicted at higher rotational speeds and this may be because of the overprediction of blade deformations. The analysis clearly showed that the reason for the reduction in the thrust producing capability of the cycloidal rotor with blade flexibility may be attributed to the large nose-down elastic twisting of the blades in the upper half cylindrical section which is not compensated by a nose-up pitching in the lower half section. The inclusion of the actual blade pitch kinematics and unsteady aerodynamics was found crucial in the accurate lateral force prediction.

Nomenclature

a	Nondimensionalized location of 3/4-chord ahead of the pitching axis, η_r/c
$\bar{a_b}$	Acceleration vector of an arbitrary point on the blade
A	Cycloidal-rotor rectangular projected area, $2bR$
AR	Aspect ratio of the blades, b/c
b	Blade span
c	Blade chord
C_d	Drag coefficient
C_{d_i}	Induced drag coefficient
C_{d_0}	Profile Drag coefficient
C_l	Lift coefficient
C_{l_c}	Circulatory lift coefficient
$C_{l_{nc}}$	Noncirculatory lift coefficient
C_{l_α}	Lift curve slope
C_T	Rotor thrust coefficient, $T_{\text{Res}}/\rho A(\Omega R)^2$
e	Oswald's efficiency factor
e_g	Chordwise location of the blade c.g. ahead of the elastic axis
EI_y	Flapwise blade bending stiffness
EI_z	Lagwise blade bending stiffness
F_n, F_c	Blade normal and chordwise forces

[*] Graduate Research Assistant, moble@umd.edu

[†] Alfred Gessow Professor and Director, chopra@umd.edu

[‡] PhD Candidate, mattaboni@aero.polimi.it

[§] Assistant Professor, masarati@aero.polimi.it

American Institute of Aeronautics and Astronautics

|	
F_w, F_v	Blade forces along the radial and tangential directions in the undeformed rotating frame
F_Z, F_Y	Blade forces in the inertial frame along Z and Y axis respectively
GJ	Blade torsional stiffness
I_0	Blade rotational moment of inertia about c.g. axis
k	Reduced frequency
m	Mass per unit length of the blade
M	Mass matrix
M_ϕ	Blade pitching moment in the undeformed frame
N_b	Number of blades
P	Blade aerodynamic power
$\bar{r}$	Position vector of an arbitrary point on the deformed blade
R	Radius of the cyclorotor
s	Non-dimensional distance traveled by the airfoil in semi-chords
t	Blade thickness for the flat plate blades
T_{DU}	Transformation matrix from an undeformed to deformed coordinate system
T_{Res}	Resultant thrust
T_u, T_d	Upstream and downstream thrust in the double multiple streamtube inflow model
T_z, T_y	Rotor thrust in the inertial frame along X and Y axis respectively, N
U_P	Velocity component normal to the blade chord
U_T	Velocity component tangential to the blade chord
v	Blade tangential bending deformation
v_i	Induced velocity in the uniform inflow model
v_u, v_d	Upstream and downstream induced velocities in the double multiple streamtube inflow model
$\bar{V}_b$	Velocity vector of an arbitrary point on the blade
$\bar{V}_w$	Wind velocity vector at an arbitrary location on the blade
w	Blade radial bending deformation, wake velocity in multiple streamtube model
x_ξ, y_η, z_ζ	Blade deformed coordinate system
$X(\hat{I}), Y(\hat{J}), Z(\hat{K})$	Cyclorotor non-rotating inertial coordinate system
$X(s), Y(s)$	Circulatory deficiency functions
$X_R(\hat{i}), Y_R(\hat{j}), Z_R(\hat{k})$	Cyclorotor undeformed rotating coordinate system
α	Quasi-steady blade section angle of attack
α_e	Unsteady effective angle of attack
β	Phase angle subtended by the resultant thrust vector with vertical
η, ζ	Coordinates parallel and normal to the blade chord in the deformed blade coordinate
η_r	Chordwise location of 3/4-chord ahead of the pitching axis
Ω	Rotational speed of the rotor
$\phi(s)$	Wagner function
$\hat{\phi}$	Blade sectional elastic twist
ρ	Air density
Ψ	Azimuthal location
θ	Rigid blade pitch angle
θ_1	Effective sectional geometric angle, $\theta + \hat{\phi}$
Superscript	
I	Inertial forces
A	Aerodynamic forces

I.   Introduction

In recent years, there has been a growing interest in a new class of very small flight vehicles called micro-air-vehicles (MAVs), which are intended for reconnaissance in confined and hazardous spaces. As the battlegrounds of the future move to restricted, highly populated urban environments, MAVs may appear to be extremely useful assets to the military. MAVs can also be used for civilian applications such as biochemical sensing, traffic monitoring, border surveillance, fire and rescue operations, wildlife surveys, power-line inspection, and real-estate aerial photography, just to name a few. Several fixed-wing MAVs have

American Institute of Aeronautics and Astronautics

already been successfully tested [1–5]. One particular example [4, 5] has a weight of 80 grams and a flight endurance of about 30 minutes. Even though fixed-wing MAVs may be the best performers today in terms of the imposed size and weight constraints, they lack the ability to hover or to operate in highly constrained environments. It is quite important to develop an efficient hover-capable highly maneuverable MAV with an expanded flight envelope. To this end, several hovering-capable MAVs based on single main rotor or coaxial rotor configurations have been successfully built and flight-tested [6–8]. However, these MAVs operate in the blade chord Reynolds number range from 10,000 to 60,000, and so they suffer from the aerodynamic inefficiencies of small scale. In fact, most MAVs based on conventional rotors have shown relatively low performance, e.g., the maximum figure of merit achieved to date is only about 0.65 [6].
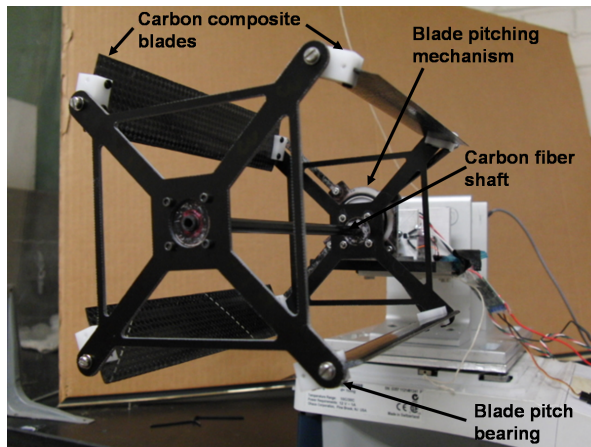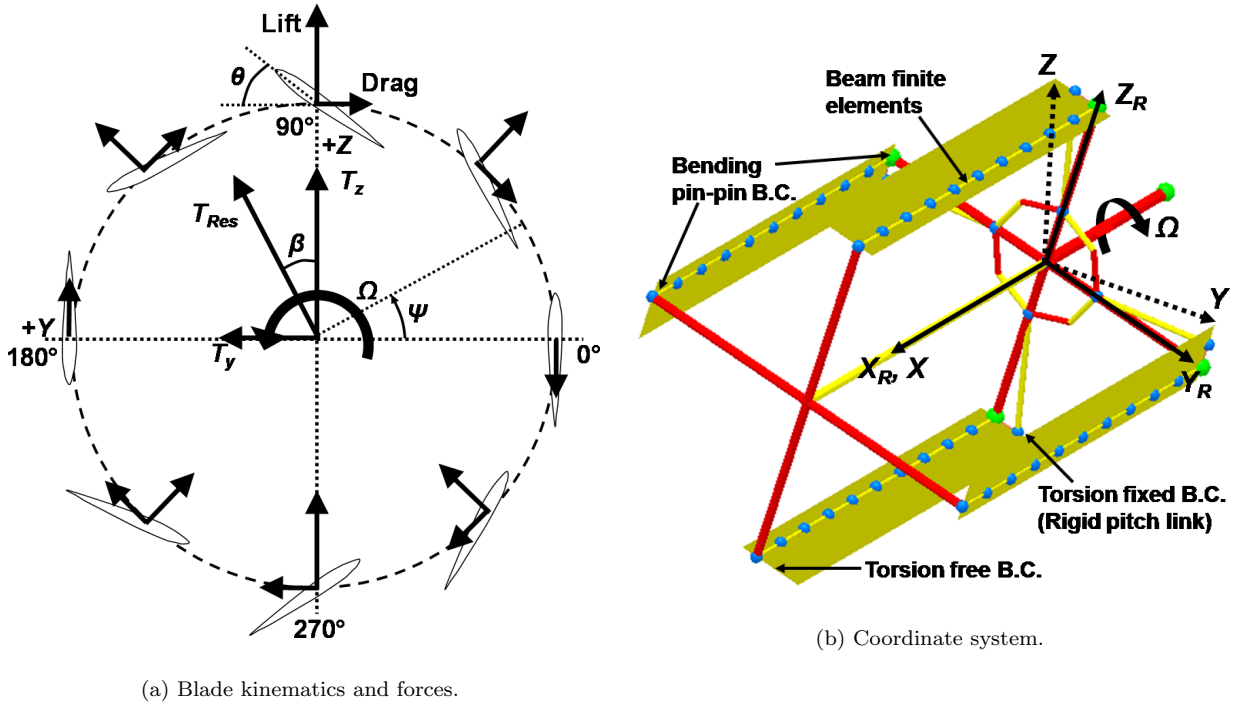

(a) 4-bladed Cyclorotor.
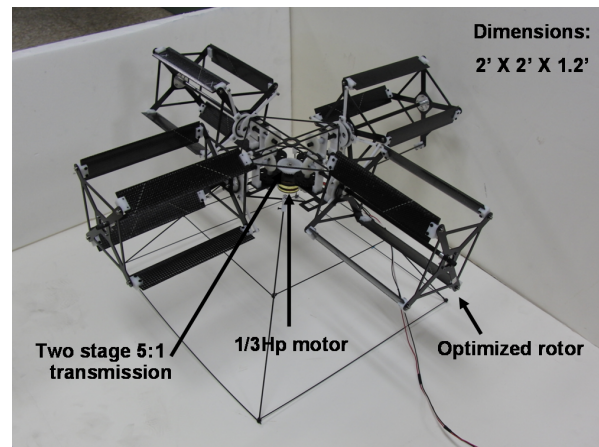
(b) Quad-rotor Cyclocopter.

Figure 1. Cyclocopter.

A MAV concept based on a cycloidal rotor (cyclorotor) system has been proposed as an alternative to a conventional rotor-based MAV. Figure 1(a) shows an isolated cyclorotor and Fig. 1(b) shows a hover capable quad-cyclocopter that has been recently built [9]. A cyclorotor (also known as a cyclocopter or cyclogiro) is a rotating-wing system where the span of the blades runs parallel to the axis of its rotation. The pitch angle of each of the blades is varied cyclically by mechanical means such that the blades experiences positive angles of attack at both the top and bottom positions of the azimuth cycle (Fig. 2(a)). The resulting time-varying lift and drag forces produced by each blade can be resolved into the vertical and horizontal directions, as shown in Fig. 2(a). Varying the amplitude and phase of the cyclic blade pitch can be used to change the magnitude and direction of the net thrust vector produced by the cyclorotor.

Compared to a conventional rotor, each spanwise blade element of a cyclorotor operates at similar aerodynamic conditions (i.e., at similar flow velocities, Reynolds numbers, and angles of incidence), and so the blades can be optimized to achieve the best aerodynamic efficiency. Moreover, because the blades are cyclically pitched once per revolution (1/rev), unsteady flow mechanisms may delay blade stall onset and in turn may augment the lift produced by the blades. Recent tests on a MAV-scale cyclorotor indicated that this concept can be aerodynamically more efficient than a conventional rotor at the lower Reynolds numbers at which MAVs operate [9–14]. Furthermore, because the thrust vector of a cyclorotor can be instantaneously set to any direction perpendicular to the rotational axis, a cyclorotor-based MAV may ultimately show better maneuverability and agility as compared to a MAV powered by a conventional rotor system, which are particularly important attributes for constrained indoor flight operations. One major drawback of a cyclorotor is its relatively large rotating structure which might offer a weight penalty when compared to a conventional rotor.

Most of the previous studies on cyclorotors have been experimental in nature and also performed at relatively larger scales [15–29]. The key conclusions from these studies are summarized in Ref. [12]. One of the initial analytical studies on cyclorotors was performed by Wheatley [19, 20] in 1930s, and it focused on the development of a simplified aerodynamic model which was validated against wind tunnel measurements. However, the analysis showed poor agreement with the experimental measurements. McNabb [25] developed

American Institute of Aeronautics and Astronautics

(a) Blade kinematics and forces.

(b) Coordinate system.

Figure 2. Cyclorotor blade kinematics, forces and coordinate system definition.

an unsteady aerodynamic model of a cyclorotor, and the predictions were found to correlate well with the measurements. More recently, Kim et al. [15–18] developed an aerodynamic model for a cyclorotor and a parallel analysis was conducted using CFD to help predict the aerodynamic characteristics. However, all these studies were performed on large-scale rotors at Reynolds numbers of the order of 10^5 or higher. The only low Reynolds number computational study was conducted by Iosilevskii and Levy [27], who performed a 2-D CFD investigation of a cyclorotor operating at blade chord Reynolds numbers of about 40,000. This CFD study helped expose the complex aerodynamic interactions between the rotating blades, which also showed good agreement with the measured time-averaged forces.

Since all these studies were focussed on developing aerodynamic models, the effects of the blade deformations were not included while calculating the aerodynamic performance. However, experimental studies have shown that at higher rotating speeds, the cycloidal rotors experience large inertial (mostly centrifugal force) and aerodynamic forces causing significant bending and torsional deformation especially for flexible blades. These deformations play a crucial role in the aerodynamic performance of the cycloidal rotor both in terms of thrust and power. Some of the results from the previous studies [12] are shown in Fig. 3. It can be clearly seen that the average thrust produced by the cyclorotor reduces as the bending and torsional stiffness of the blade is decreased. Therefore, the effect of deformations cannot be neglected for the evaluation of the performance of the cyclorotor. The goal of the present study is to develop a refined aeroelastic model to predict the performance of a MAV-scale cyclorotor.

The structural modeling of the cyclorotor blade is performed using two parallel approaches, (1) non-linear finite element analysis for a beam undergoing radial bending, tangential bending and twisting motions and, (2) multibody based analysis using a full-nonlinear beam model suitable for extremely flexible blades that undergo large displacements. Even though for the moderately flexible blades, the finite element model was able to predict the deformations accurately, for the extremely flexible blades, a full-nonlinear model based analysis may be important to predict the deformations correctly [30]. The structural model is then coupled with an unsteady aerodynamic model which uses two different inflow models, uniform inflow and a double-multiple streamtube (D-MS) based inflow model. Finally, the thrust predicted by the aeroelastic models will be validated with the experimental measurements for moderately flexible and flexible blades.
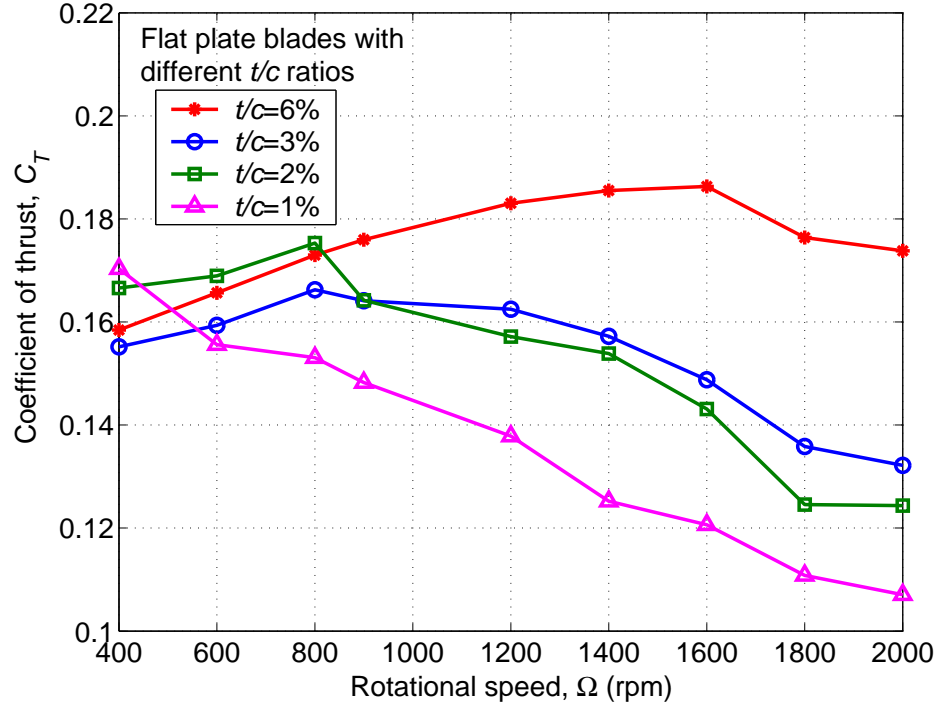
American Institute of Aeronautics and Astronautics

Figure 3. Effect of flexibility on cyclorotor thrust coefficient (C_T).

II.   Analysis Methodologies

In the present study, two completely independent aeroelastic models have been developed to predict the performance of a MAV-scale cyclorotor. The first model uses a structural model based on non-linear finite element analysis for a beam undergoing radial bending, tangential bending and torsional degrees of freedom with an unsteady aerodynamic model and two different inflow models, uniform inflow and double-multiple streamtube (D-MS) model. The steady blade periodic response is obtained using a finite element in time approach. However, this model can be only used for moderate blade deformations. Therefore, a second model was developed using a multibody based analysis (using the software MBDyn) for the structural model so that it can handle large deformations. The aerodynamic formulation is same as the previous model except that it uses a state space formulation for the unsteady loads calculation. For the remainder of the paper, the first model will be referred to as the FEM analysis and the second model as MBDyn.

A.   FEM Based Aeroelastic Analysis

1.   Rotor structural model

The cyclorotor blades are modeled as non-linear, isotropic Euler-Bernoulli beam undergoing radial bending (flap, w), tangential bending (lag, v) and elastic twist (ϕ) deformations. The definitions of radial bending, tangential bending and torsional deformations are shown in Figs. 4(a) and 4(b). The coupled flap-lag-torsion equations are based on Ref. [31] and can handle moderate deformations since the model includes geometric non-linearities up to second order. Each blade is modeled using 10 finite elements undergoing flap, lag and torsional degrees of freedom. The cyclorotor blades were assumed to have a pin-pin boundary conditions for bending and a fixed-free boundary condition for torsion (Fig. 2(b)). Torsion has a fixed boundary condition at the root because the pitching linkages are assumed to be rigid. In the present study, three different composite laminated blades were analyzed, which included a baseline NACA 0010 carbon blade, 6% thickness-to-chord ratio (t/c) flat plate carbon blade, and 3% t/c flexible flat plate carbon blade. All the blades had uniform chord of 1 inch and span of 6 inches. Detailed structural testing was conducted to obtain the bending and torsional stiffness (EI_y, EI_z and GJ) of the blades. The structural properties of the different blades are provided in Table. 1. The equations of motion for the blade is developed using Hamilton's principle. To

obtain the steady blade periodic response the governing partial differential equations are solved using finite element method in time.

Table 1. Blade structural properties

Blade	$EI_y(N-m^2)$	$EI_z(N-m^2)$	$GJ(N-m^2)$	$m(Kg/m)$	c.g location from LE
Baseline NACA 0010	0.19	2.9	0.25	0.025	40%c
6% flat plate	0.40	102	0.12	0.061	50%c
3% flat plate	0.026	29	0.01	0.022	50%c

(a) Forces
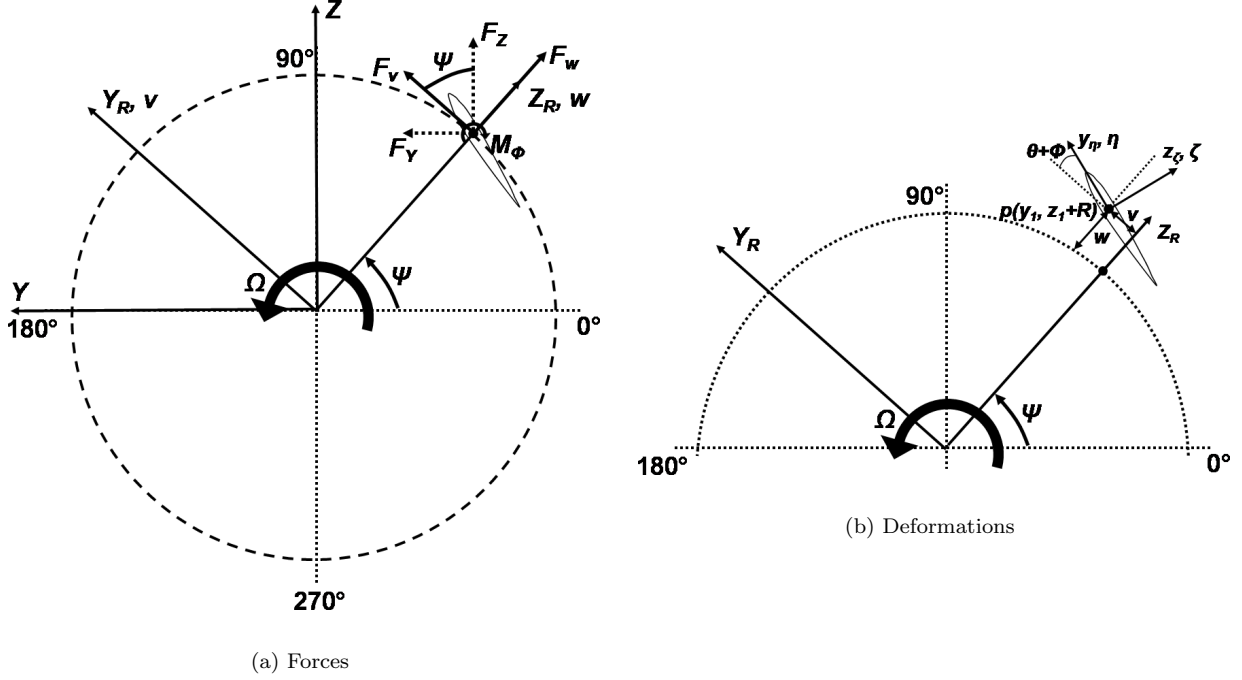
(b) Deformations

Figure 4. Definition of forces and deformations on a cyclorotor.

2. Inertial force formulation

Figures 2(b) and 4(a) shows the coordinate system and the definition of the inertial forces on a cycloidal rotor. Let the position of an arbitrary point on the deformed beam be given by the position vector $\bar{r}$ which is given by:

$$\bar{r} = x_1\hat{i} + y_1\hat{j} + (z_1 + R)\hat{k}, \tag{1}$$

where $\hat{i}$, $\hat{j}$ and $\hat{k}$ are the unit vectors along along the rotating undeformed coordinate system (X_R, Y_R, Z_R). x_1, y_1 and z_1 can be expressed as

$$
\begin{aligned}
x_1 &= x - v'(y_1 - v) - w'(z_1 - w), \\
y_1 &= v + (y_1 - v), \\
z_1 &= w + (z_1 - w),
\end{aligned}
\tag{2}
$$

and

$$
\begin{aligned}
y_1 - v &= \eta\cos\theta_1 - \zeta\sin\theta_1, \\
z_1 - w &= \eta\sin\theta_1 + \zeta\cos\theta_1,
\end{aligned}
\tag{3}
$$

American Institute of Aeronautics and Astronautics

$$\theta_1 = \theta + \hat{\phi}. \tag{4}$$

Now, the velocity vector, $\bar{V}_b$ is given as:

$$\bar{V}_b = \frac{\partial \bar{r}}{\partial t} + \bar{\Omega} \times \bar{r}, \tag{5}$$

where

$$\bar{\Omega} = -\Omega \hat{i}, \tag{6}$$

and

$$\frac{\partial \bar{r}}{\partial t} = \dot{x}_1 \hat{i} + \dot{y}_1 \hat{j} + \dot{z}_1 \hat{k}. \tag{7}$$

For the present blades $\eta = e_g$ and $\zeta = 0$, where e_g is the chordwise location of the blade c.g. ahead of the elastic axis. For instance, if the blade elastic axis is at 1/4-chord and the blade c.g. is at 1/2-chord, then $e_g = -0.25c$.

$$\dot{x}_1 = -(\dot{v}' + w'\dot{\theta}_1)e_g \cos\theta_1 - (\dot{w}' - v'\dot{\theta}_1)e_g \sin\theta_1, \tag{8}$$

$$\dot{y}_1 = \dot{v} - e_g \sin\theta_1 \dot{\theta}_1, \tag{9}$$

$$\dot{z}_1 = \dot{w} + e_g \cos\theta_1 \dot{\theta}_1, \tag{10}$$

$$\bar{V}_b = V_{bx}\hat{i} + V_{by}\hat{j} + (V_{bz})\hat{k}, \tag{11}$$

$$V_{bx} = -(\dot{v}' + w'\dot{\theta}_1)e_g \cos\theta_1 - (\dot{w}' - v'\dot{\theta}_1)e_g \sin\theta_1, \tag{12}$$

$$V_{by} = \dot{v} - e_g \sin\theta_1 \dot{\theta}_1 + \Omega(w + e_g \sin\theta_1 + R), \tag{13}$$

$$V_{bz} = \dot{w} + e_g \cos\theta_1 \dot{\theta}_1 - \Omega(v + e_g \cos\theta_1). \tag{14}$$

Now the acceleration of the point (x_1, y_1, z_1) on the blade is given by:

$$\bar{a}_b = \frac{\partial^2 \bar{r}}{\partial t^2} + \bar{\Omega} \times (\bar{\Omega} \times \bar{r}) + 2\bar{\Omega} \times \frac{\partial \bar{r}}{\partial t}, \tag{15}$$

$$\frac{\partial^2 \bar{r}}{\partial t^2} = \ddot{x}_1 \hat{i} + \ddot{y}_1 \hat{j} + \ddot{z}_1 \hat{k}, \tag{16}$$

$$\ddot{x}_1 = -e_g \cos\theta_1(\ddot{v}' + w'\ddot{\theta}_1 + \dot{w}'\dot{\theta}_1) + (\dot{v}' + w'\dot{\theta}_1)e_g \sin\theta_1 \dot{\theta}_1 - e_g \sin\theta_1(\ddot{w}' - v'\ddot{\theta}_1 - \dot{v}'\dot{\theta}_1) - (\dot{w}' - v'\dot{\theta}_1)e_g \cos\theta_1 \dot{\theta}_1, \tag{17}$$

$$\ddot{y}_1 = \ddot{v} - e_g \sin\theta_1 \ddot{\theta}_1 - \dot{\theta}_1^2 e_g \cos\theta_1, \tag{18}$$

$$\ddot{z}_1 = \ddot{w} + e_g \cos\theta_1 \ddot{\theta}_1 - \dot{\theta}_1^2 e_g \sin\theta_1. \tag{19}$$

From eqns 15 – 19, the inertial forces in the flap (F_w^I), lag (F_v^I) and torsion (M_ϕ^I) direction are given as:

$$F_w^I = -m[\ddot{w} + e_g \cos\theta_1 \ddot{\theta}_1 - \dot{\theta}_1^2 e_g \sin\theta_1 - \Omega^2(w + e_g \sin\theta_1 + R) - 2\Omega(\dot{v} - e_g \sin\theta_1 \dot{\theta}_1)], \tag{20}$$

$$F_v^I = -m[\ddot{v} - e_g \sin\theta_1 \ddot{\theta}_1 - \dot{\theta}_1^2 e_g \cos\theta_1 - \Omega^2(v + e_g \cos\theta_1) + 2\Omega(\dot{w} + e_g \cos\theta_1 \dot{\theta}_1)], \tag{21}$$

$$M_\phi^I = -me_g[-\ddot{v}\sin\theta_1 + \ddot{w}\cos\theta_1 - 2\Omega(\dot{w}\sin\theta_1 + \dot{v}\cos\theta_1) - \Omega^2 \cos\theta_1(w + R) + \Omega^2 \sin\theta_1 v] - I_0\ddot{\theta}_1. \tag{22}$$

B. Multibody Model

In modeling a non-conventional system, such as the cyclorotor, the multibody approach appears attractive because it provides the opportunity to build hierarchically models of increasing complexity. This attribute has been exploited in this work, where first of all an aeroelastic model of a single blade has been realized and validated, then the same blade has been used to model 2-, 3-, 4-, and 5-bladed rotors. Subsequently, the model complexity was increased through an addition of a kinematically exact model of the blades 1/rev pitching mechanism. Within the multibody formalism, the latter is been added using the elements of the joints library to reproduce the actual joints of the pitching mechanism.

A multibody model of the cyclorotor has been realized using the general-purpose open-source multibody simulation software MBDyn. MBDyn provides the availability of many working elements, together with the possibility to add new elements. In the present work this possibility has been exploited to add some aerodynamics features fundamental for the cyclorotor modeling, such as the unsteady aerodynamics model based on indicial aerodynamics and the inflow models for this unconventional rotor.
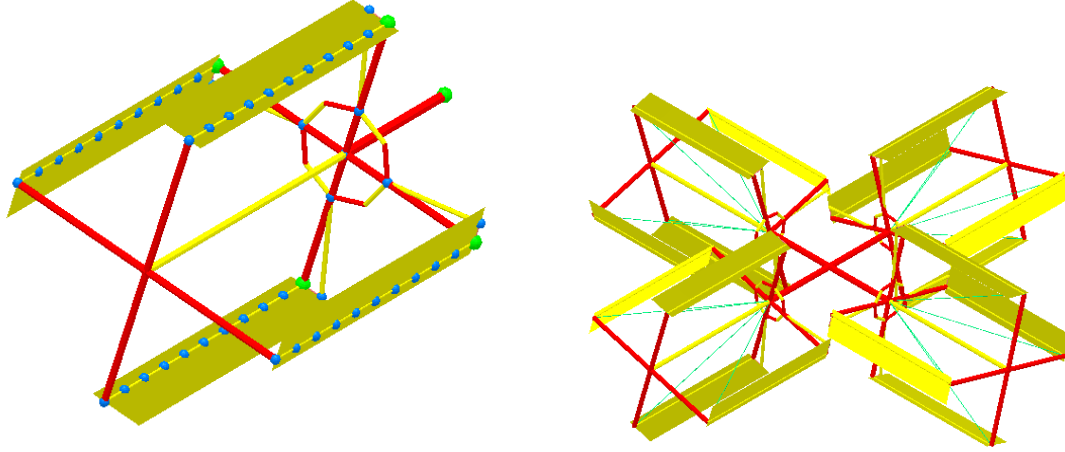
American Institute of Aeronautics and Astronautics

Figure 5. Multibody models.

1. The multibody solver MBDyn

MBDyn is a software intended to model generic multidisciplinary problems, characterized by exact constrained rigid body dynamics, deformable components, simplified aerodynamics, and vehicle controls. It solves Initial Value Problems (IVP) in form of Differential-Algebraic Equations (DAE),using a family of multistep L-stable integration algorithms.

The dynamics of the rigid bodies is written in term of Newton-Euler equations, constrained using Lagrange's multipliers. The equations of motion of all the unconstrained nodes can be summarized as:

$$\mathbf{M}\dot{\mathbf{q}} = \mathbf{p} \tag{23}$$
$$\dot{\mathbf{p}} = \mathbf{f}\left(\mathbf{q}, \dot{\mathbf{q}}, \mathbf{p}, t\right),$$

where $\mathbf{q} \in \mathbb{R}^n$ summarizes the n coordinates of the system, $\mathbf{M} \in \mathbb{R}^{n \times n}$ is the mass matrix, $\mathbf{p} \in \mathbb{R}^n$ summarizes the momentum and momenta moments and $\mathbf{f} : \mathbb{R}^{3n+1} \mapsto \mathbb{R}^n$ summarizes the generic forces, possibly depending on the configuration of the system.

When the system is subjected to kinematics constraints, the c constraint equations $\phi\left(\mathbf{q}, t\right) : \mathbb{R}^{n+1} \mapsto \mathbb{R}^n$ are added to Eqs. 23 using Lagrange's multipliers, resulting in:

$$\mathbf{M}\dot{\mathbf{q}} = \mathbf{p} \tag{24}$$
$$\dot{\mathbf{p}} + \phi_{/\mathbf{q}}^T \boldsymbol{\lambda} = \mathbf{f}\left(\mathbf{q}, \dot{\mathbf{q}}, \mathbf{p}, t\right)$$
$$\phi\left(\mathbf{q}, t\right) = \mathbf{0}.$$

Eqs. 24 express the dynamics of a system constrained by holonomic rheonomic constraints in form of implicit DAE:

$$\mathbf{g}\left(\dot{\mathbf{y}}, \mathbf{y}, t\right) = \mathbf{0}, \tag{25}$$

where $\mathbf{y} = \left[\mathbf{q}^T, \mathbf{p}^T, \boldsymbol{\lambda}^T\right]^T$ summarizes all the variables in Eqs. 24. The DAE is solved using original multistep integration algorithms described in Ref. [30].

2. Structural modeling

The cycloidal rotor's blades are modeled using 5 three-nodes beam elements. MBDyn implements an original non-linear finite-volume geometrically exact beam formulation, described in Ref. [35]. This beam model can simulate large node displacements that arise when the blade is very flexible and the rotor speed is high.

(a) Pitching amplitude=30°.

(b) Pitching amplitude=40°.
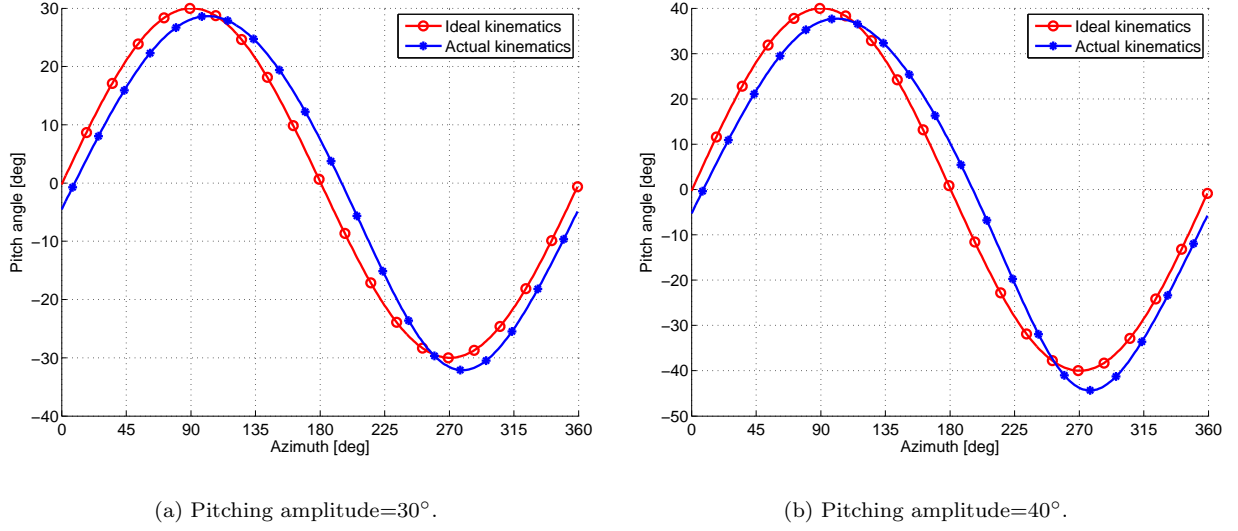
Figure 6. Actual pitch versus ideal pitch.

The blade is constrained in two points: a spherical hinge at the blade root and a spherical hinge free to move along the blade span at the tip. The blade pitch is imposed in two different ways:

1. Ideal kinematics: the desired pitch angle is directly imposed to the blade root, so it is possible to have an arbitrary relationship between the pitch angle θ and the blade azimuth ψ.

2. Actual kinematics: the actual pitching mechanism is modeled in order to obtain the actual pitch angle. In this case the relationship $\theta = f(\psi)$ is fixed and depends only on the mechanism geometry.

Figure. 6 shows the comparison of the ideal harmonic blade pitching kinematics with the actual kinematics obtained using MBDyn for 30° and 40° pitching amplitudes. In the FEM analysis the actual blade kinematics was included using a four-bar based blade kinematics analysis. One key characteristic to note in Fig. 6 is the phase delay in the actual kinematics with respect to the ideal kinematics and this is one reason for the lateral force production.

As said in the previous section MBDyn solves initial value problems, so a dynamics simulation with a fictitious initial transient starting from a null rotor speed is performed to obtain the final periodic solution.

C. Aerodynamic Modeling

Flowfield studies have clearly shown that the cycloidal rotor blades operate in a complex 3-D aerodynamic environment characterized by unsteady effects such as dynamic stall resulting from the large amplitude blade pitching at high reduced frequencies ($k \approx 0.18$) [13]. A higher fidelity modeling tool such as CFD would be required to capture all these effects with sufficient accuracy. However, in the present study, the goal is to develop a low-order model which can predict the blade loads and average rotor performance with sufficient accuracy so that it could be used for routine design calculations. Therefore, a blade element based aerodynamic model using an unsteady attached flow formulation (thin airfoil theory) is used in the present analysis. Unsteady aerodynamics formulation uses indicial aerodynamics based on Wagner function and Duhamel's superposition principle to obtain the circulatory lift and moment for arbitrary variations in angle of attack. It should be noted that the use of Wagner function is an approximation for the present problem since the wake from the trailing edge of the airfoil is not planar.

It is important to justify the use of an attached flow formulation without a stall model when the blades are pitching at high amplitudes. First of all, none of the previous experiments have showed any evidence of blade stall until a pitching amplitude of 40° [12,13]. One reason for this is the large induced velocities, as measured in the rotor wake using PIV, which clearly shows that the actual aerodynamic angle of attack is much lower than the pitch angle [12]. Another reason could be the fact that the unsteady effects normally delay the stall

American Institute of Aeronautics and Astronautics

(a) Blade pitching amplitude=25°.

(b) Blade pitching amplitude=30°.
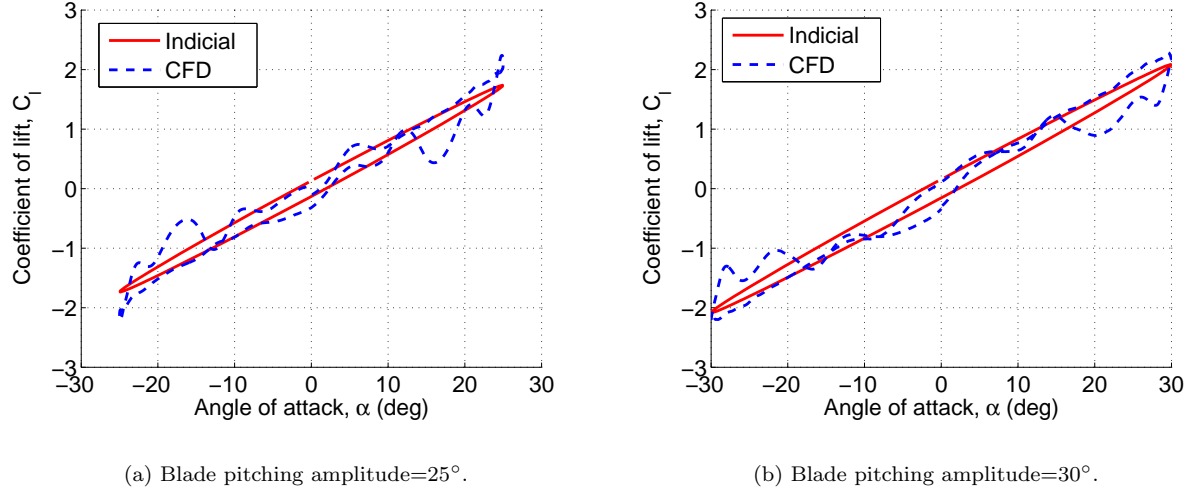
Figure 7. Comparison of lift coefficient (C_l) from attached indicial model with 2-D CFD results for a NACA 0010 airfoil pitching in freestream, Re=25,000, reduced frequency, k=0.18.

to higher angle of attacks. Therefore, to understand the role of unsteady aerodynamics on the lift produced by an airfoil at these low Reynolds numbers, a 2-D CFD analysis was performed on an airfoil pitching in a uniform freestream. The airfoil was harmonically pitched ($\alpha = \alpha_0 sin(\Omega t)$) in a uniform freestream at a reduced frequency of 0.18 and Reynolds number = 25,000. Figures 7(a) and 7(b) show variation of C_l with α for NACA 0010 airfoil predicted using 2-D CFD for pitching amplitudes of 25° and 30°, respectively. It was interesting to see that at these low Reynolds numbers, even at such high pitching amplitudes, the dynamic stall was extremely weak and this was mainly because of the continuous shedding of vorticity from the airfoil leading edge (evident from the local dips in C_l curve), instead of vorticity accumulation at the leading edge and shedding as a strong dynamic stall vortex as expected in conventional dynamic stall at high Reynolds numbers. Because of this reason, as shown in Figs. 7(a) and 7(b), the attached flow indicial aerodynamics formulation with a C_{l_α} of 5.1 is able to predict the average behavior reasonably well which might be sufficient to predict the average forces correctly. However, it should be noted that this is an approximation and a better way of modeling this would be by using a dynamic stall model such as the Leishman-Beddoes model.

1. Inflow model

An accurate inflow model is the key to predicting the aerodynamic loads on the cyclorotor. Two different inflow models based on momentum theory are examined in the present study, 1) Uniform inflow model where the entire rotor is immersed in a single stream tube as shown in Fig. 8(a), 2) A Double-Multiple streamtube (D-MS) model developed in Ref. [15], where the rotor is divided into number of streamtubes and also the influence of the upper half of the rotor on the lower half is taken into account (Fig. 8(b)).

2. Uniform inflow model

For the uniform inflow model, the magnitude of the inflow is calculated as

$$v_i = \sqrt{\frac{T}{2\rho A}} \tag{26}$$

The direction of the inflow is updated in each iteration based on the direction of the resultant thrust (β) as shown in Fig. 8(a).

American Institute of Aeronautics and Astronautics

(a) Uniform inflow.

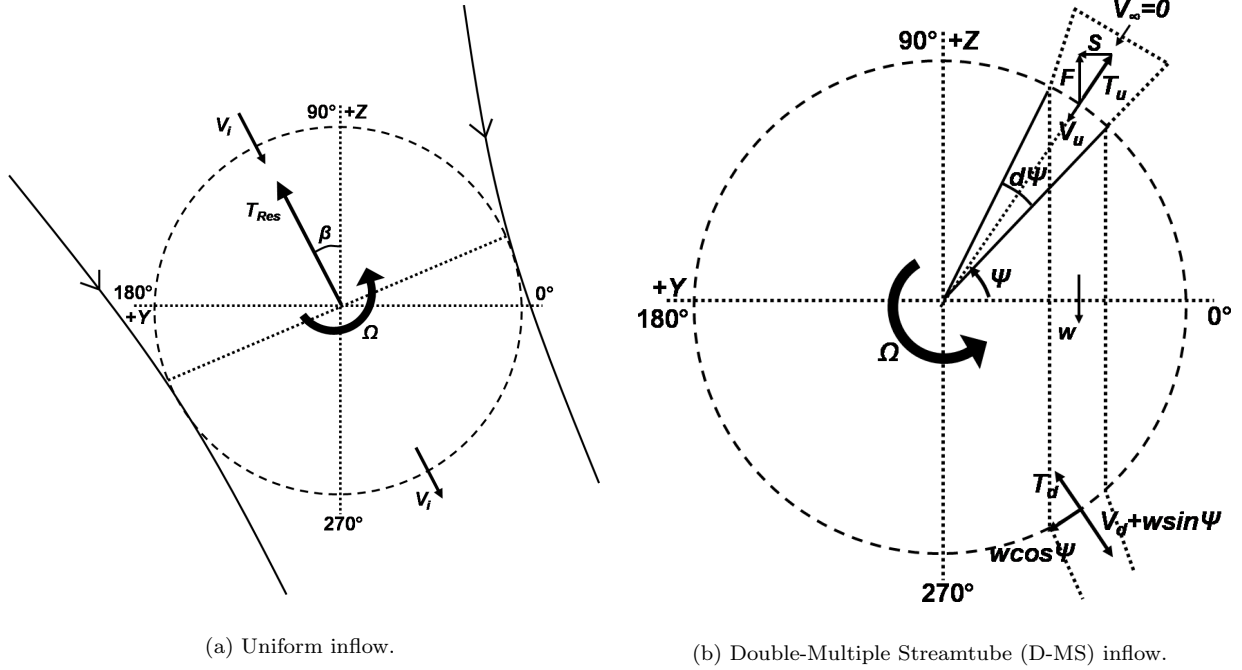(b) Double-Multiple Streamtube (D-MS) inflow.

Figure 8. Schematic of the inflow models.

3. Double-Multiple Streamtube (D-MS) inflow model

In the multiple streamtube model, the rotor is divided into a number of streamtubes, which intersect the rotor twice with different induced velocity values at the upstream and downstream halves as shown in Fig. 8(b). At the two points of intersection of each streamtube with the blade path, the blade swept area ($Rd\psi$) acts as infinitesimally thin actuator surfaces, across which the rotor imparts axial momentum into the flow. In the present formulation, this 2-D inflow model has to be used at each spanwise location of the blade since the angle of attack of the blade and hence the lift produced varies along the span due to elastic blade twist.

In the upstream half, the flow enters the rotor in the radial direction and bends due to the pressure forces ($\bar{S}$) from the adjacent streamtube so that the streamtube becomes vertical. The bending of the streamtube is also important to maintain the symmetry of the flow inside the rotor. It is also assumed that the freestream pressure is attained at some point inside the rotor and the velocity at that point is taken as the wake velocity (w) for the upstream actuator surface. The wake velocity forms the freestream velocity to the downstream actuator surface. Based on the mass, momentum and energy conservation in the streamtube, the wake velocity can be expressed in terms of the upstream induced velocity as:

$$w = \frac{2v_u}{\sin \Psi}, \tag{27}$$

where

$$v_u = \sqrt{\frac{dT_u \sin^2 \Psi}{2\rho R d\Psi}} \tag{28}$$

For the downstream half of the rotor:

$$dT_d = 2\rho R v_d \sqrt{w^2 + 2wv_d \sin \Psi + v_d^2} d\Psi \tag{29}$$

The above equation has to be iteratively solved to obtain the inflow v_d in the downstream half. $dT_{u,d}$ is given by

$$dT_{u,d} = \bar{F}_w^A \left(\frac{N_b d\Psi}{2\pi} \right) \tag{30}$$

where $\bar{F}_w^A$ is the aerodynamic force in the radial direction which will be derived later in the paper. Equation 30 is derived based on the assumption that for a cyclorotor with N_b blades, each of these N_b blades spends $(d\Psi/2\pi)$ time in each streamtube.
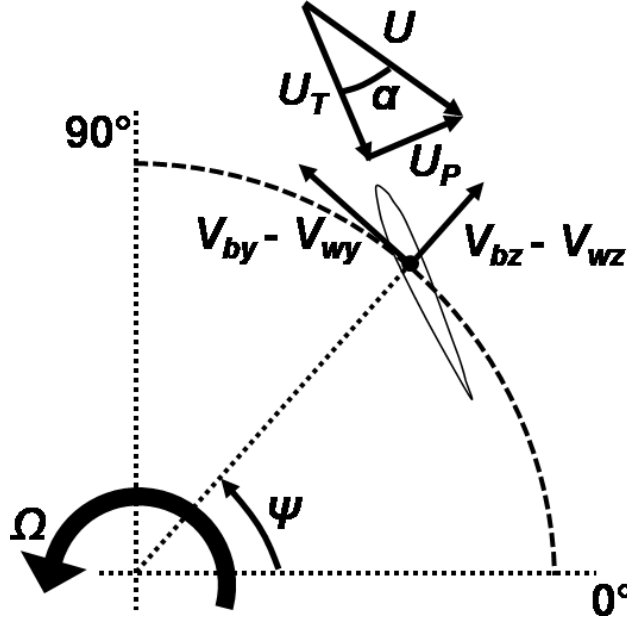

Figure 9. Schematic showing the velocities used in the aerodynamics formulation.

4. Calculation of blade aerodynamic loads

First step in the calculation of the blade aerodynamic forces is the calculation of section angle of attack. The angle of attack of a blade segment is due to two components: the wind velocity and the blade velocity at the 3/4 chord location. The general expression for the resultant velocity at a spanwise station, x, in the rotating undeformed frame is given by (Fig. 9):

$$\bar{V} = -\bar{V}_w + \bar{V}_b, \tag{31}$$

where $\bar{V}_w$ is the wind velocity contribution from rotor inflow and $\bar{V}_b$ is the blade velocity relative to the hub fixed frame resulting from blade rotation and blade motion:

$$\bar{V}_w = V_{wx}\hat{i} + V_{wy}\hat{j} + V_{wz}\hat{k}. \tag{32}$$

For the uniform inflow model:

$$
\begin{aligned}
V_{wx} &= 0, \\
V_{wy} &= -v_i \cos(\Psi - \beta), \\
V_{wz} &= -v_i \sin(\Psi - \beta).
\end{aligned}
\tag{33}
$$

For the multiple streamtube inflow model upstream half:

$$
\begin{aligned}
V_{wx} &= 0, \\
V_{wy} &= 0, \\
V_{wz} &= -v_u,
\end{aligned}
\tag{34}
$$

and for the downstream half:

$$
\begin{aligned}
V_{wx} &= 0, \\
V_{wy} &= -w \cos\Psi, \\
V_{wz} &= w \sin\Psi + v_d.
\end{aligned}
\tag{35}
$$

The blade velocities V_{bx}, V_{by} and V_{bz} are given in Eqns. 12–14. However, since the blade velocities are calculated at 3/4-chord, the distance e_g is replaced by η_r, where η_r is the position of the 3/4-chord location ahead of the blade pitching axis. For instance, if the blade is pitching at 1/4-chord, $\eta_r = -0.5c$.

$$
\begin{aligned}
V_{bx} &= -(\dot{v}' + w'\dot{\theta}_1)\eta_r \cos\theta_1 - (\dot{w}' - v'\dot{\theta}_1)\eta_r \sin\theta_1, \\
V_{by} &= \dot{v} - \eta_r \sin\theta_1 \dot{\theta}_1 + \Omega(w + \eta_r \sin\theta_1 + R), \\
V_{bz} &= \dot{w} + \eta_r \cos\theta_1 \dot{\theta}_1 - \Omega(v + \eta_r \cos\theta_1).
\end{aligned}
\tag{36}
$$

The resultant blade velocity at a spanwise location, x, can be written in the rotating undeformed coordinate system as:

$$
\bar{V} = V_x \hat{i} + V_y \hat{j} + V_z \hat{k} = (V_{bx} - V_{wx})\hat{i} + (V_{by} - V_{wy})\hat{j} + (V_{bz} - V_{wz})\hat{k}.
\tag{37}
$$

However, the blade section loads are calculated using the resultant velocity and aerodynamic angle of attack in the rotating deformed blade coordinate system:

$$
\begin{bmatrix} U_R \\ U_T \\ U_P \end{bmatrix} = T_{DU} \begin{bmatrix} V_x \\ V_y \\ V_z \end{bmatrix},
\tag{38}
$$

where U_R, U_T and U_P are the velocities in the deformed frame (Fig. 9) and T_{DU} is the transformation matrix from undeformed to deformed frame:

$$
T_{DU} = \begin{bmatrix}
1 - \frac{v'^2}{2} - \frac{w'^2}{2} & v' & w' \\
-v'\cos\theta_1 - w'\sin\theta_1 & \left(1 - \frac{v'^2}{2}\right)\cos\theta_1 - v'w'\sin\theta_1 & \left(1 - \frac{w'^2}{2}\right)\sin\theta_1 \\
v'\sin\theta_1 - w'\cos\theta_1 & -\left(1 - \frac{v'^2}{2}\right)\sin\theta_1 - v'w'\cos\theta_1 & \left(1 - \frac{w'^2}{2}\right)\cos\theta_1
\end{bmatrix},
\tag{39}
$$

$$
\alpha = \tan^{-1}\left(\frac{U_P}{U_T}\right),
\tag{40}
$$

$$
U = \sqrt{U_T^2 + U_P^2}.
\tag{41}
$$

Wagner function based indicial aerodynamics is used to include the unsteady effects [36,37]. In this formulation, the angle of attack variation over time is discretized as a series of step inputs. The airload response to each step input is calculated using semi-empirical indicial response functions. The response depends on the pitch and pitch rate of each step input. Once the indicial response is known, the unsteady loads to arbitrary changes in angle of attack can be obtained through the superposition of indicial aerodynamic responses using the Duhamel's integral. The circulatory part of the lift coefficient, C_l^c, in response to an arbitrary variation in angle of attack can be now written in terms of Wagner function ($\phi(s)$) as:

$$
C_l^c(t) = 2\pi\left(\alpha(0)\phi(s) + \int_0^s \frac{d\alpha(\sigma)}{dt}\phi(s - \sigma)d\sigma\right) = 2\pi\alpha_e(t),
\tag{42}
$$

where α_e represents the effective angle of attack and contains within it all of the time history effects on the lift because of the shed wake,

$$
s = \frac{2}{c}\int_0^t U dt.
\tag{43}
$$

The approximate expression for Wagner function for incompressible flow is given by:

$$
\phi(s) \approx 1 - A_1 e^{-b_1 s} - A_2 e^{-b_2 s},
\tag{44}
$$

where $A_1 = 0.165$, $A_2 = 0.335$, $b_1 = 0.0455$ and $b_2 = 0.3$. The Duhamel's integral is solved in a recursive fashion and the effective unsteady angle of attack (α_e) is given as:

$$
\alpha_e = \alpha - X(s) - Y(s),
\tag{45}
$$

where $X(s)$ and $Y(s)$ are the deficiency functions, which are obtained numerically using one step recursive formulas given below:

$$X(s) = X(s - \delta s)e^{-b_1 \Delta s} + A_1 \Delta \alpha_s,$$
$$Y(s) = Y(s - \delta s)e^{-b_2 \Delta s} + A_2 \Delta \alpha_s. \tag{46}$$

The sectional lift and moment coefficients includes the contribution from both circulatory and non-circulatory components:

$$C_l = C_l^c + C_l^{nc}, \tag{47}$$
$$C_m = C_m^c + C_m^{nc}. \tag{48}$$

The circulatory and non-circulatory components of lift are expressed as:

$$C_l^c = C_{l_\alpha} \alpha_e,$$
$$C_l^{nc} = \frac{\pi}{2U} c\dot{\alpha} - \frac{\pi}{4}\left(\frac{c}{U}\right)^2 a\ddot{\alpha}. \tag{49}$$

The circulatory and non-circulatory components of moment are expressed as:

$$C_m^c = \frac{1}{2}C_{l_\alpha}(a + 0.5)\alpha_e,$$
$$C_m^{nc} = \frac{\pi c}{4}\left(-\frac{1}{V}(0.5 - a)\dot{\alpha} - \frac{c}{2V^2}\left(\frac{1}{8} + a^2\right)\ddot{\alpha}\right). \tag{50}$$

For the present formulation, since the pitching axis is at 1/4-chord, a=-0.5. As explained in previous section, for the present analysis, C_{l_α} of 5.1 is used. Sectional profile drag is given by:

$$C_{d_0} = d_0 + d_1\alpha + d_2\alpha^2. \tag{51}$$

Based on the 2-D CFD study, the static C_{d_0} values for a NACA 0010 airfoil at 25,000 Reynolds number could be approximately expressed using $d_0 = 0.0334$, $d_1 = 0$ (symmetric airfoil) and $d_2 = 2.511$. The total drag, C_d, is given as the sum of profile (C_{d_0}) and induced drag (C_{d_i}) components:

$$C_d = C_{d_0} + C_{d_i}, \tag{52}$$

where C_{d_i} is given as:

$$C_{d_i} = \frac{C_l^2}{\pi ARe}. \tag{53}$$

In the present analysis the Oswald's efficiency factor, e is assumed to be 0.85. The normal (F_n^A) and chordwise (F_c^A) forces and the pitching moment (M_ϕ^A) are given as:

$$F_n^A = 0.5\rho U^2 c(C_l \cos \alpha + C_d \sin \alpha), \tag{54}$$
$$F_c^A = 0.5\rho U^2 c(C_l \sin \alpha - C_d \cos \alpha), \tag{55}$$
$$M_\phi^A = 0.5\rho U^2 c^2 C_m. \tag{56}$$

In the present formulation, spanwise flow is ignored and therefore the force in the spanwise direction, $F_x^A = 0$. Aerodynamic forces in the undeformed rotating blade coordinate system is given by:

$$\bar{F}^A = F_u^A \hat{i} + F_v^A \hat{j} + F_w^A \hat{k}, \tag{57}$$

where

$$\begin{bmatrix} F_u^A \\ F_v^A \\ F_w^A \end{bmatrix} = T_{DU}^T \begin{bmatrix} F_x^A \\ F_c^A \\ F_n^A \end{bmatrix}. \tag{58}$$

The aerodynamic forces in the non-rotating inertial frame, F_Z^A and F_Y^A is given by:

$$F_Z^A = F_w^A \sin \Psi + F_v^A \cos \Psi, \tag{59}$$
$$F_Y^A = -F_w^A \cos \Psi + F_v^A \sin \Psi. \tag{60}$$

The instantaneous power required to rotate the blade is by:

$$P = -F_v^A(\Omega R). \tag{61}$$

American Institute of Aeronautics and Astronautics

D. Validation of the Structural Model and Inertial Force Formulation in the FEM Analysis

The structural model along with the inertial forces in the FEM analysis have been validated by comparing the deformations predicted by the FEM analysis with the results obtained from the multibody model due to only inertial forces for moderate deformations as shown in Figs 10(a) to 10(f). Figure 10(a) shows the comparison of the FEM analysis with MBDyn for the variation of mid-beam radial bending deformation around the azimuth for a pitching amplitude of 30° (harmonic pitching) at a rotational speed of 2000 rpm for the baseline NACA 0010 blade which is relatively stiffer than the other blades tested. Figures 10(c) and 10(e), respectively, show the comparison of the tangential bending and tip torsional deformation for the same case. Figures 10(b), 10(d) and 10(f) shows the validation of deformation for a pitching amplitude of 40° and 2000 rpm. It can be clearly seen that there is an overall satisfactory agreement between the FEM analysis and multibody based analysis for moderate deformations. However it was observed that for the extremely flexible blades (3% flat plate carbon blade), the FEM model is not able to predict the deformations accurately. This clearly shows the need for a full nonlinear beam modeling tool such as the one available in MBDyn in order to be able to accurately predict the performance of extremely flexible blades.

E. Validation of the Aerodynamic Model

Since only the average forces were measured during the experiments, the force predictions obtained from a 3-D CFD study [32] was used to validate the instantaneous forces from the unsteady aerodynamic model based on the two different inflow models: (1) Uniform inflow, and (2) Double-Multiple streamtube (D-MS) model. For validation studies, rigid blades (no deformations) were used in both CFD and the present analysis so that the aerodynamic model can be validated independent of the structural model.

Figures 11(a) and 11(b), respectively, shows the comparison between CFD, uniform inflow and multiple streamtube model for the instantaneous vertical (T_z) and lateral aerodynamic forces (T_y) in the inertial frame produced by a single blade on a 2-bladed cyclorotor using rigid blades at a pitching amplitude of 35°. It can be clearly seen that the forces predicted by the multiple streamtube model show better agreement with CFD predicted forces especially in the case of the vertical force (T_z). However, the uniform inflow model underpredicts T_z in the upper half of the blade trajectory and overpredicts in the lower half. In the case of lateral force (T_y), the multiple streamtube model shows satisfactory agreement with the CFD predicted forces. However, it will be shown later that even though the uniform inflow does not predict the instantaneous forces accurately, the average forces are captured well using the uniform inflow model.

The other interesting characteristic to note from the time history is that, even though the blade pitch angle is identical at the top most ($\psi=90°$) and bottom most ($\psi=270°$) points of the blade trajectory, the vertical force (T_z) at the top most point is almost half of that at the bottom. Even if there is an effect of the wake from the upper half on the lower half, it should only decrease the angle of attack at the bottom half and thereby decrease the vertical force. However, the opposite is happening because of the virtual camber effect caused due to the flow curvature, which will reduce the effective C_l at the upper half [14, 33]. The virtual camber effect will be taken into account if the angle of attack is calculated at 3/4-chord location [34]. Figure. 12 clearly shows the effect of virtual camber and inflow on the lift variation on the blades. The dotted line in the figure shows the variation of lift coefficient of the blade calculated based on pure geometric pitch angle. Because of the large chord-to-radius ratio of the present cyclorotor, when the virtual camber effect is included, there is a downward shift of the curve (dashed line), increasing the magnitude of the lift in the lower half and decreasing the lift in the upper half. Inclusion of the inflow effect (solid line) using the double-multiple streamtube model, tries to reduce the lift in the lower half since it operates in the wake of the upper half. Even then, it can be clearly seen that the magnitude of the lift coefficient is much higher in the lower half compared to the upper half. This is the reason for the higher vertical thrust in the lower half compared to the upper half.

From figures 10(a) to 10(f) it can be seen that even for the relatively stiff, NACA 0010 blades, there was a small difference in bending and torsional deformations between the FEM and multibody analysis. Now, the next step was to investigate whether these small differences in deformations can cause significant differences in the aerodynamic forces and also to validate the aerodynamic models in the FEM and multibody analysis. Figure 13 clearly shows that even with the small differences in the deformation predictions, the aerodynamic forces match perfectly. However, this is not true for the flexible 3% carbon blades because the deformations predicted by MBDyn and the FEM analysis are significantly different. Therefore, for the flexible blades, the analysis was only performed using MBDyn.
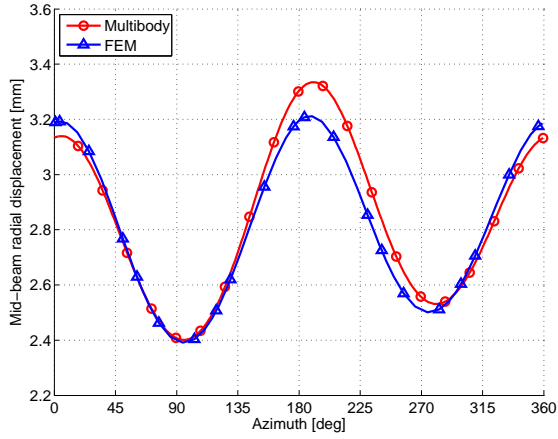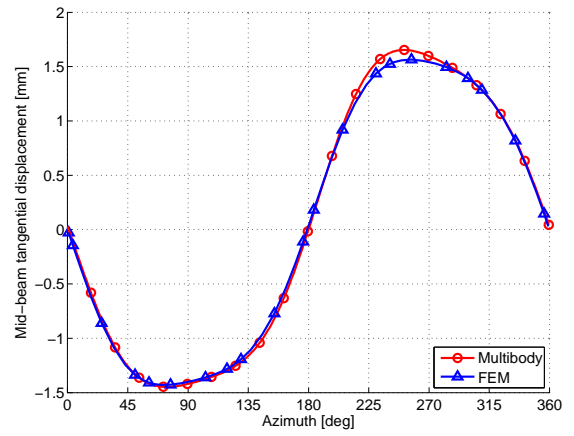
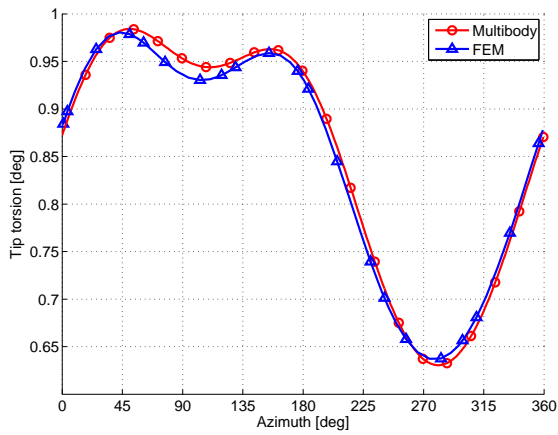(a) Mid-beam radial bending deformation (w) for NACA 0010 blades at 30° pitching amplitude.
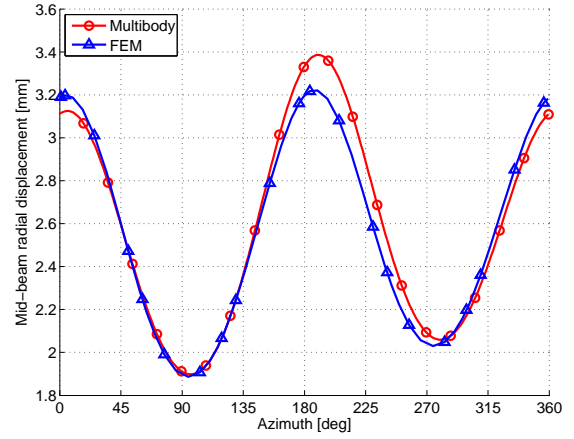
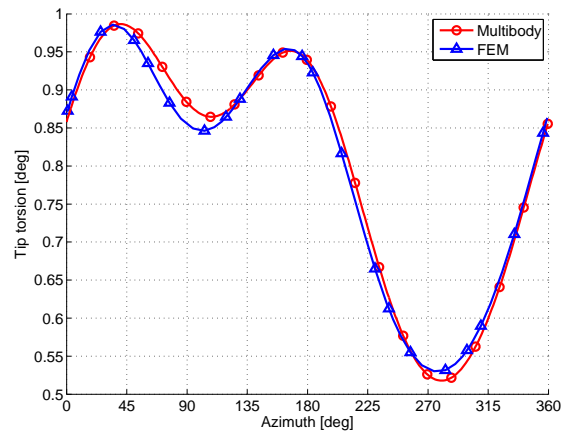(b) Mid-beam radial bending deformation (w) for NACA 0010 blades at 40° pitching amplitude.
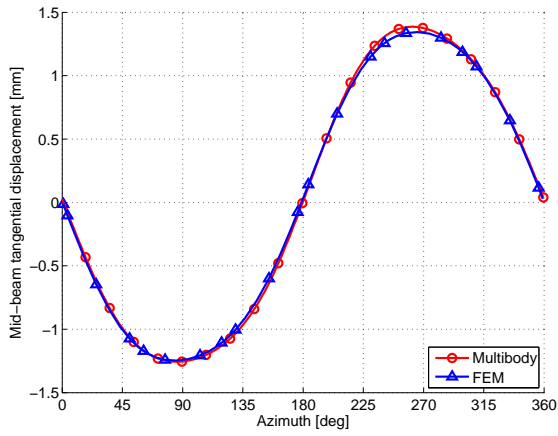
(c) Mid-beam tangential bending deformation (v) for NACA 0010 blades at 30° pitching amplitude.

(d) Mid-beam tangential bending deformation (v) for NACA 0010 blades at 40° pitching amplitude.

(e) Tip torsional deformation (ϕ) for NACA 0010 blades at 30° pitching amplitude.

(f) Tip torsional deformation (ϕ) for NACA 0010 blades at 40° pitching amplitude.

Figure 10. Comparison of FEM and MBDyn blade deformations with inertial loads for the baseline NACA 0010 blades at 2000 rpm.

American Institute of Aeronautics and Astronautics

(a) Vertical force, T_z

(b) Lateral force, T_y
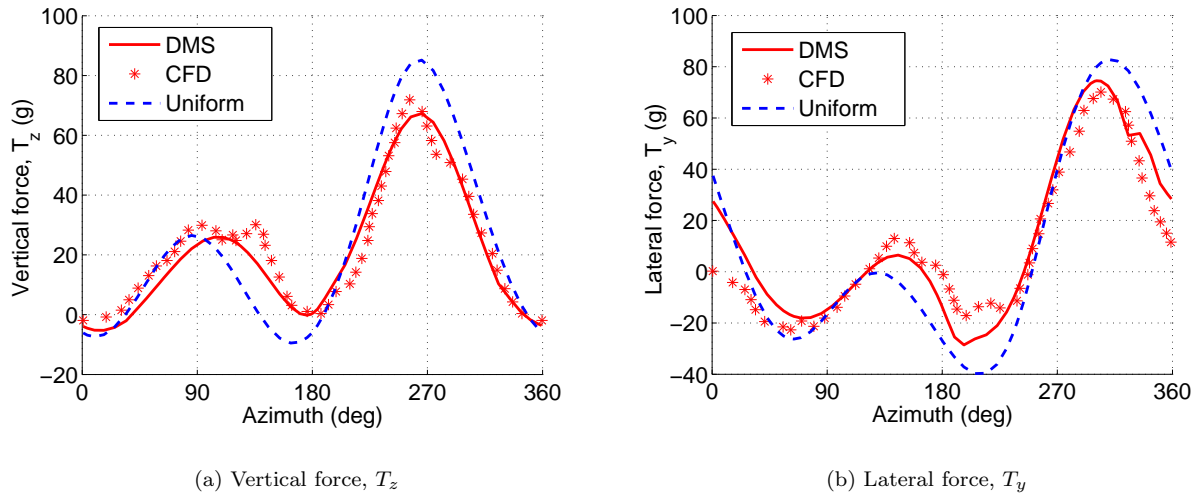
Figure 11. Comparison of the instantaneous vertical (T_z) and lateral (T_y) aerodynamic forces in the inertial frame due to a single blade with 3-D CFD results at a pitching amplitude of $35°$ for a **2-bladed rotor with rigid blades using uniform inflow and double-multiple streamtube (D-MS) inflow models.**
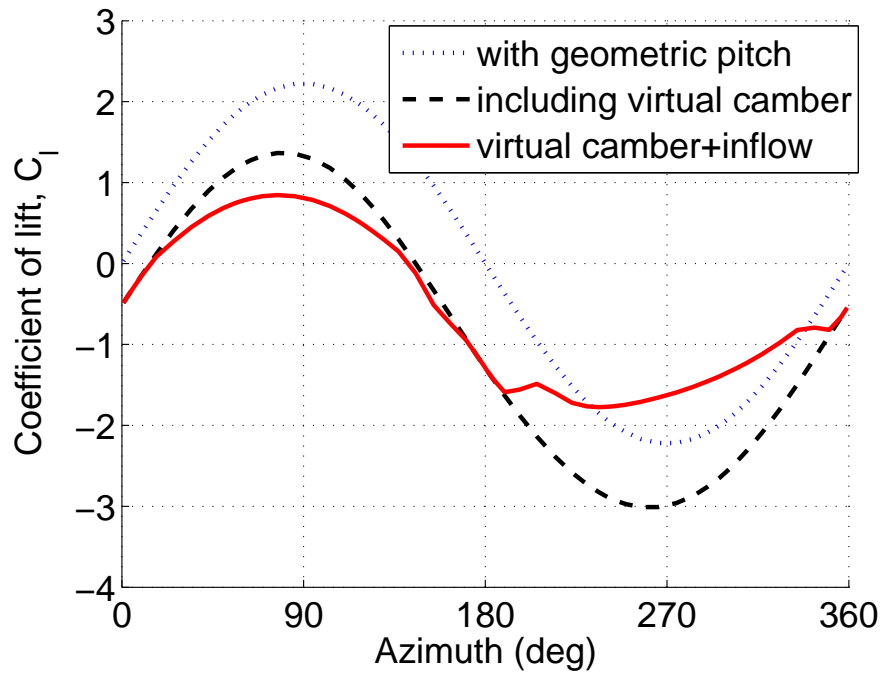
Figure 12. Effect of virtual camber effect and inflow on the blade lift.
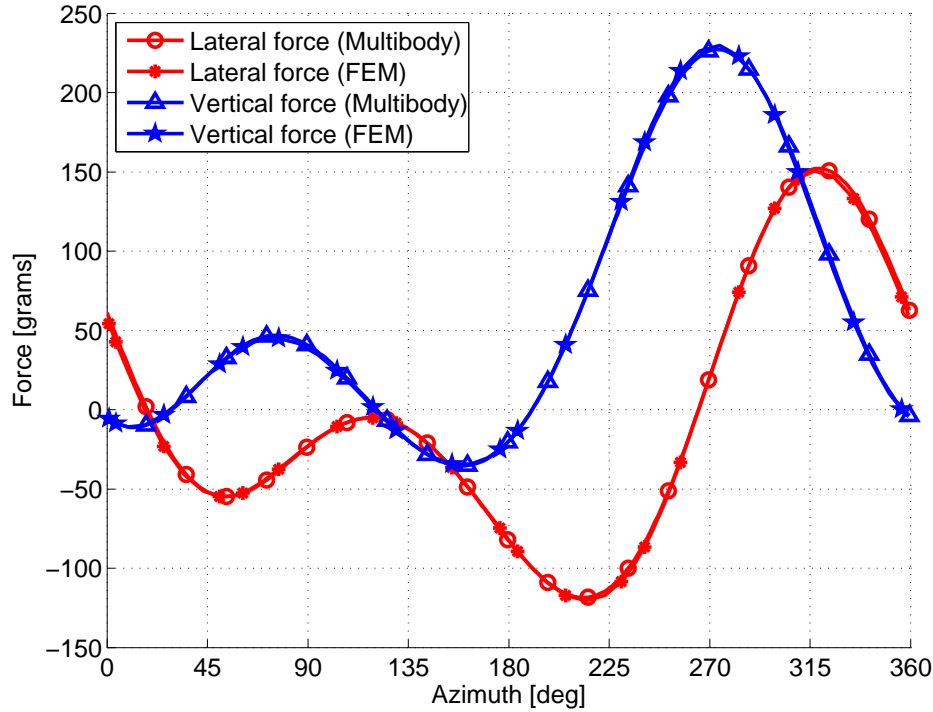
Figure 13. Comparison of the instantaneous vertical (T_z) and lateral (T_y) aerodynamic forces for a 1-bladed rotor operating at $30°$ pitching amplitude (harmonic pitching) using NACA 0010 blade.

F.   Effect of Aerodynamics on Blade Deformation

Understanding the contribution of aerodynamic forces to the blade deformation is the key in deciding whether a coupled aeroelastic analysis is required to accurately predict the blade aerodynamic loads; or it is acceptable to obtain the deformations based on just inertial loads (primarily centrifugal force) and provide it as prescribed deformations to the aerodynamic model. This understanding is of great significance while performing a CFD-CSD analysis where each iteration is extremely computationally expensive. Figures 14(a) to 14(f) show the variation of mid-blade radial bending (w), mid-blade tangential bending (v) and tip twist (ϕ) about the azimuth due to inertial loads and combined inertial and aerodynamic loads for 3% flexible carbon blade and baseline NACA 0010 blade at $40°$ pitching amplitude obtained using MBDyn with uniform inflow aerodynamic model. It can be clearly seen from the figures that for both the blades, even though the deformations were primarily driven by the inertial forces, the addition of aerodynamic forces brought in significant differences especially for radial bending and torsional deformation. However, for the stiffer NACA 0010 blades, since the deformations themselves are significantly small, the effect of these deformations on aerodynamic forces will be minimal. This clearly proves that a coupled aeroelastic analysis is required in order to be able to predict the blade aerodynamic loads accurately, especially for flexible blades.

## G.   Effect of Unsteady Aerodynamics

Since the blades are operating at a relatively high reduced frequency ($k \approx 0.18$), the unsteady aerodynamic effects can have a significant effect on the blade loads. However, the most significant effect of the unsteady aerodynamics is in creating a phase lag in the development of aerodynamic forces which contributes to the lateral force. Figure 15 compares the predicted average vertical and lateral force with quasi-steady and unsteady aerodynamic model for $30°$ harmonic blade pitching. It can be clearly seen that the unsteady effect produced significantly higher lateral force compared to the quasi-steady model. Also, the vertical force drops slightly with the inclusion of unsteady aerodynamics.
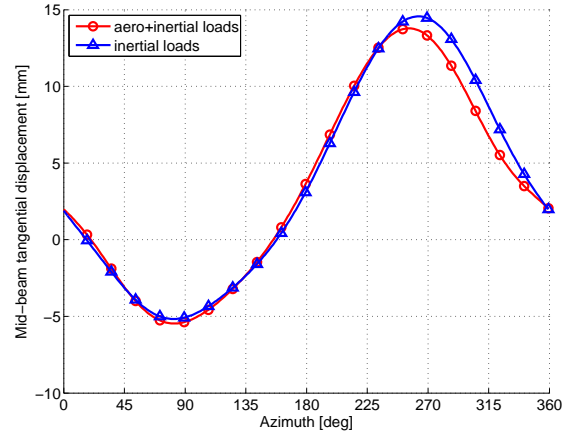
American Institute of Aeronautics and Astronautics
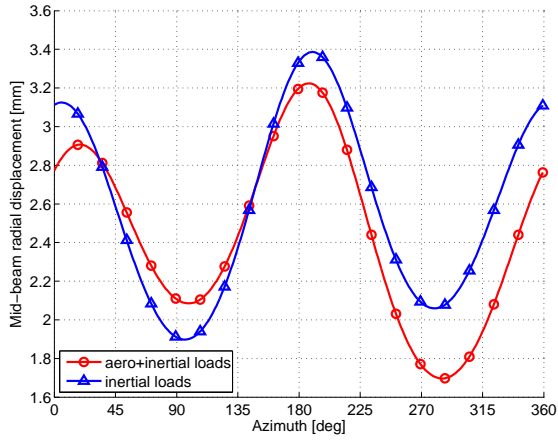
(a) Mid-beam radial bending deformation (w) for NACA 0010 blades.
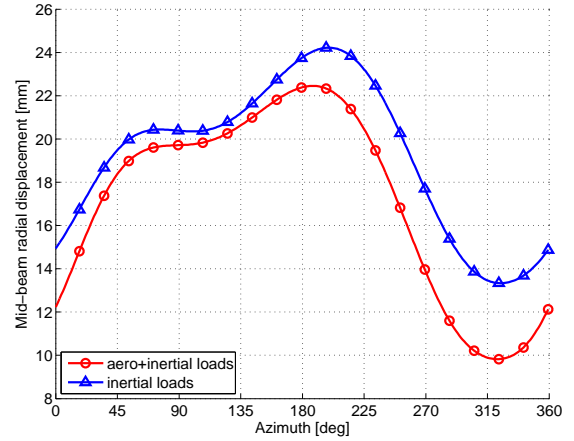
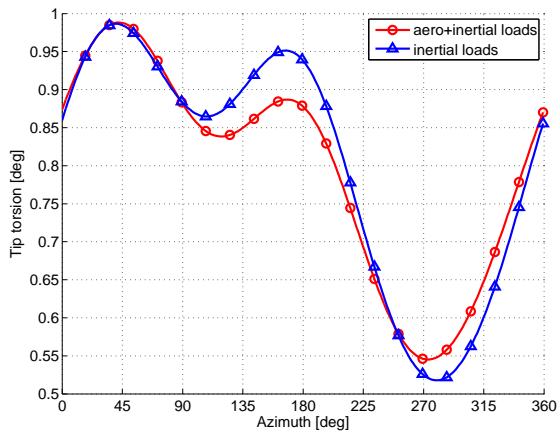(b) Mid-beam radial bending deformation (w) for 3% blades.
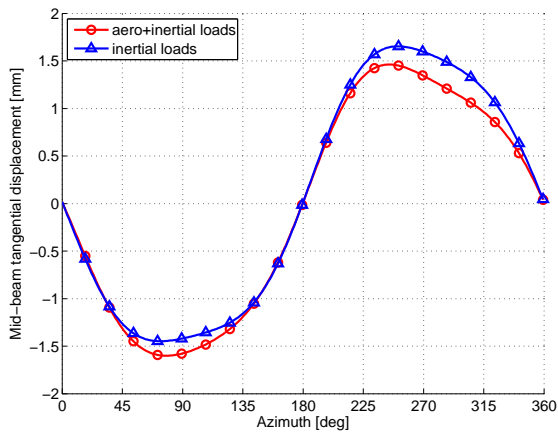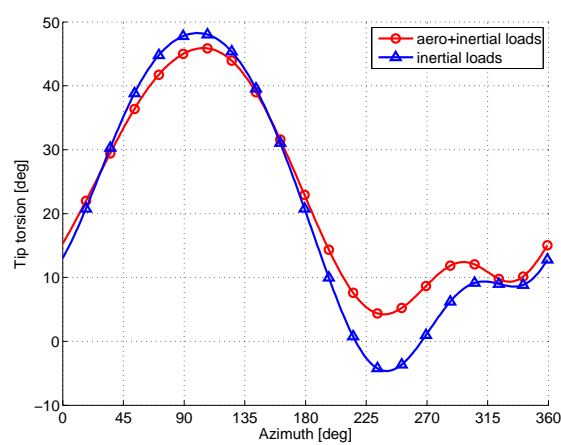
(c) Mid-beam tangential bending deformation (v) for NACA 0010 blades.

(d) Mid-beam tangential bending deformation (v) for 3% blades.

(e) Tip torsional deformation (ϕ) for NACA 0010 blades.

(f) Tip torsional deformation (ϕ) for 3% blades.

Figure 14. Comparison of blade deformations with and without aerodynamic loads for the baseline NACA 0010 blades and 3% carbon blades at $40°$ pitching amplitude and 2000 rpm.

American Institute of Aeronautics and Astronautics
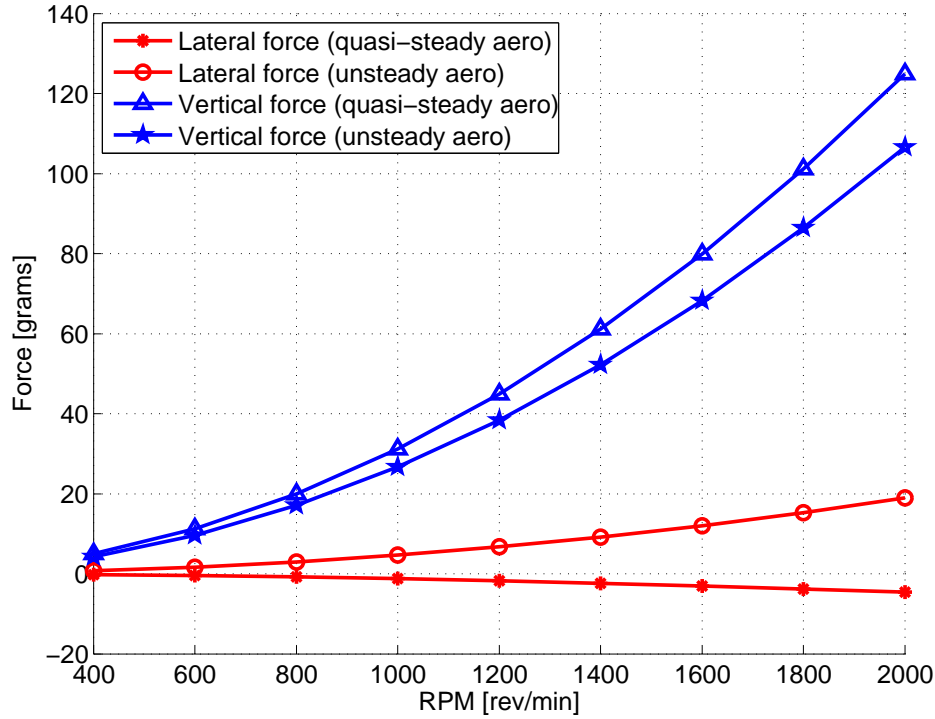
Figure 15. Comparison of the average vertical (T_z) and lateral (T_y) forces with quasi-steady and unsteady aerodynamics for a 3-bladed rotor operating at 30° harmonic pitching.

III.   Validation of the Aeroelastic Models

The two aeroelastic models: (1) Nonlinear FEM with aerodynamic model based on double multiple streamtube inflow model, and (2) Multibody with uniform inflow based aerodynamic model, were validated using the experimental results on a MAV-scale cycloidal rotor from Refs. [12, 13]. The model was validated for 2- and 3-bladed cyclorotors over a range of rotational speeds from 400 rpm to 2000 rpm and pitching amplitudes ranging from 25° to 40°. As discussed before, the blades used in the validation studies included a relatively stiffer baseline NACA 0010 carbon blade and two flat plate carbon blades which had thickness-to-chord ratios of 6% and 3%. The validation studies were performed using the actual blade pitching kinematics in the model.

A.   NACA 0010 carbon blades

For the NACA 0010 blades, as shown in Figs. 10(a) to 10(f), the deformations predicted by both the FEM analysis and MBDyn were in good agreement. Moreover, the elastic deformations were small and therefore it did not have a significant effect on the blade aerodynamic loads. Therefore, it should be noted that, for these blades, the differences between the predicted and measured forces are driven by the inaccuracies in aerodynamic modeling, and not because of the inaccurate prediction of the blade deformations. It was also shown that using the same aerodynamic model, both FEM and MBDyn predicted identical blade loads for the NACA 0010 blades (Fig. 13). Therefore, it would be more useful to compare average force predictions from the aeroelastic models based on two different inflow models with the experimentally measured forces.

Figures 16(a)– 16(d) and 17(a)– 17(d) show the validation of the vertical (T_z), lateral (T_y) and resultant force (T) for 2- and 3-bladed rotors, respectively, for four different blade pitching amplitudes. Figures 16(a) and 16(b) show the validation of T_z, T_y and T for a 2-bladed rotor operating at a pithing amplitude of 25°. It can be clearly seen that the multiple streamtube model is predicting the vertical force very accurately, however, the lateral force is underpredicted. The uniform inflow model is slightly underpredicting the vertical force, and slightly overpredicting the lateral force. However, both the models are predicting the resultant force (T) very accurately. Figures 16(c) and 16(d) show the validation for the 2-bladed cyclorotor for a
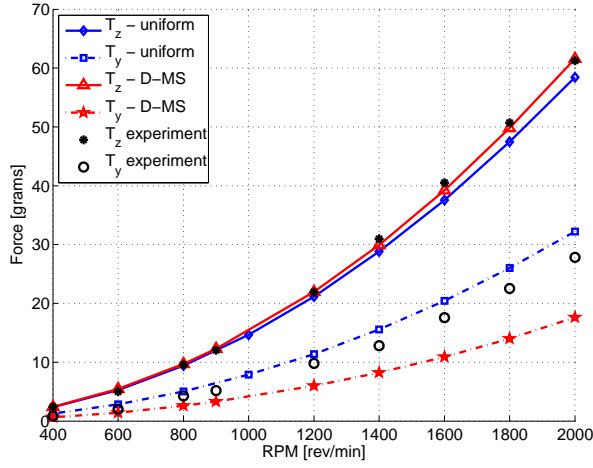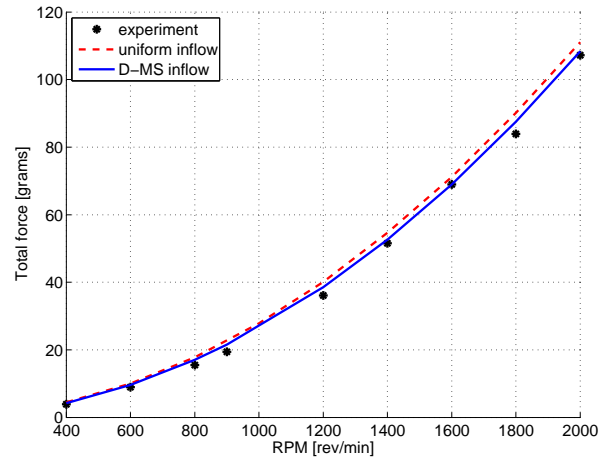
(a) T_z and T_y for blade pitching amplitude=25°.
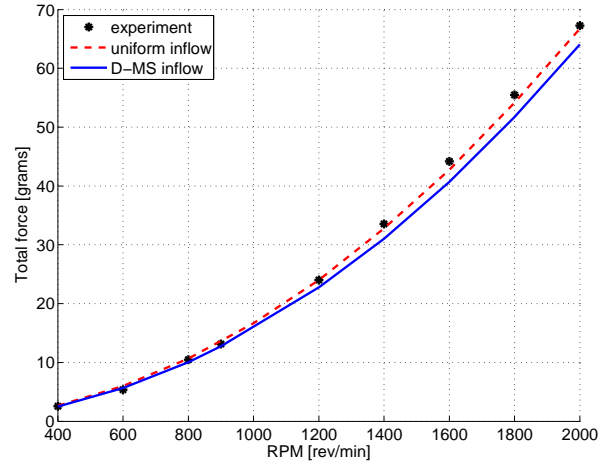
(b) Total force for blade pitching amplitude=25°.
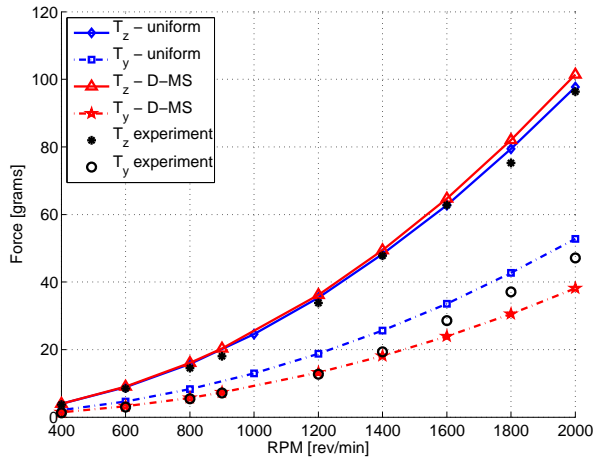
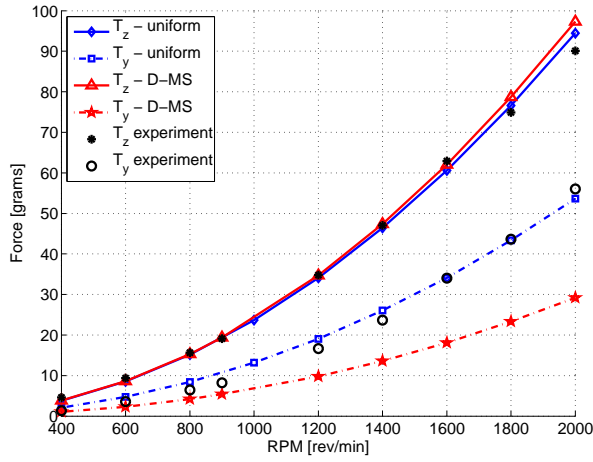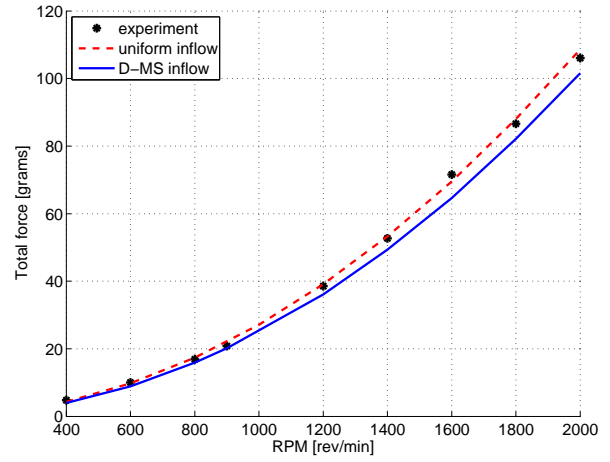(c) T_z and T_y for blade pitching amplitude=40°.
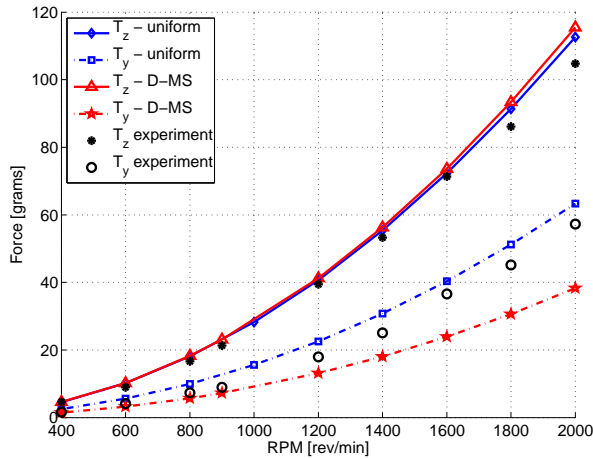
(d) Total force for blade pitching amplitude=40°.

Figure 16. Comparison of the predicted average vertical (T_z) and lateral (T_y) and total thrust (T) with experimental data for a 2-bladed rotor using NACA 0010 baseline blades.
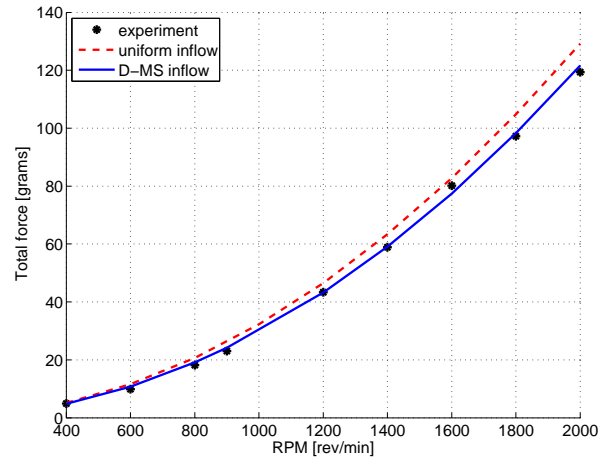
(a) T_z and T_y for blade pitching amplitude=30°.


(b) Total force for blade pitching amplitude=30°.

(c) T_z and T_y for blade pitching amplitude=35°.

(d) Total force for blade pitching amplitude=35°.

Figure 17. Comparison of the predicted average vertical (T_z) and lateral (T_y) and total thrust (T) with experimental data for a 3-bladed rotor using NACA 0010 baseline blades.

pitching amplitude of 40°. It can be clearly seen that the multiple streamtube model is predicting the lateral force very accurately till a rotational speed of 1400 rpm, however, the uniform inflow model is overpredicting the lateral force. Again as in the previous cases the resultant thrust is predicted accurately.

(a) Vertical force, T_z

(b) Lateral force, T_y
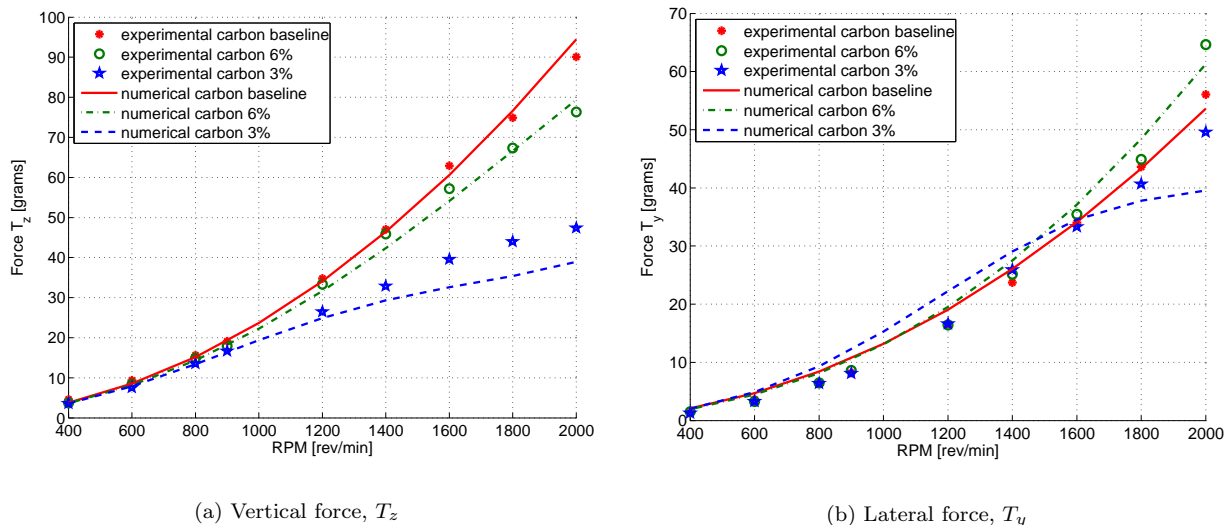
Figure 18. Comparison of the predicted average vertical (T_z) and lateral (T_y) force with experimental data at a pitching amplitude of 30° **for a 3-bladed rotor using baseline NACA blades and 6% and 3% flat plate blades.**

Figures 17(a) and 17(b) show the force validation for a 3-bladed rotor operating at 30° pithing amplitude. Again, similar to the previous case, the vertical force is predicted accurately with both the uniform inflow and multiple streamtube model, however, lateral force predictions are better with the uniform inflow model. For the 35° case (Fig. 17(c)), again both the models were equally good in predicting the vertical force even though there was a slight overprediction above 1600 rpm and the lateral force predictions from the multiple streamtube model were lower than the measured values. However, the uniform inflow model predicted the lateral force reasonably well for most of the rotational speeds even though there was a slight over prediction. Again, as in the previous cases, both the models predicted the resultant force accurately (Fig. 17(d)), and in this case the multiple streamtube model was slightly better than the uniform inflow model.

A key conclusion from the above study is that, both the inflow models are equally good in predicting the vertical and resultant forces. However, the uniform flow model predicted the lateral force better than the multiple streamtube model. The multiple streamtube model was able to predict the lateral force more accurately at higher pitch amplitudes and lower rotational speeds. From a cyclocopter design point of view, predicting the resultant thrust is very important and both the models are capable of satisfactorily predicting the magnitude of the resultant thrust. The inability of the model to predict the individual vertical and lateral forces in some of the cases means that the phasing of the resultant thrust with respect to the pitch angle is not predicted correctly.

B. Flexible flat plate carbon blades

As explained before, experimental studies have clearly shown that the thrust producing capability of the cyclorotor deteriorates as the blades are made flexible. This aspect is investigated in this section using 3% and 6% thickness-to-chord ratio flat plate blades. The results are compared with the baseline NACA 0010 blades.

Earlier, it was shown that for the relatively stiff NACA 0010 blade, the resultant thrust was predicted with sufficient accuracy with either of the aerodynamic models. However, as explained before, since the blades were relatively stiff, it was more of an aerodynamic problem. However, for the flexible blades, it is a highly coupled aeroelastic problem and the accurate prediction of both structural deformations and aerodynamic forces (with the effect of deformations) is important for the accurate prediction of the rotor thrust. Also, for the flexible blades, the present FEM analysis was not able to predict the deformations

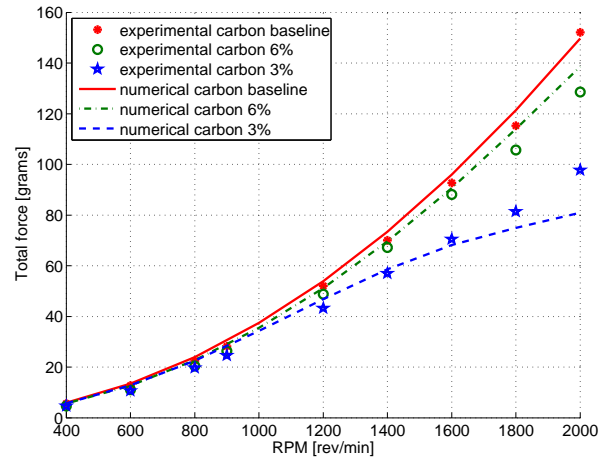American Institute of Aeronautics and Astronautics
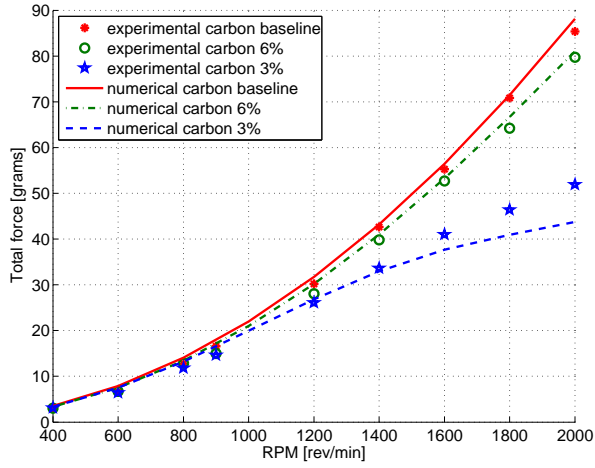
(a) Blade pitching amplitude=25°
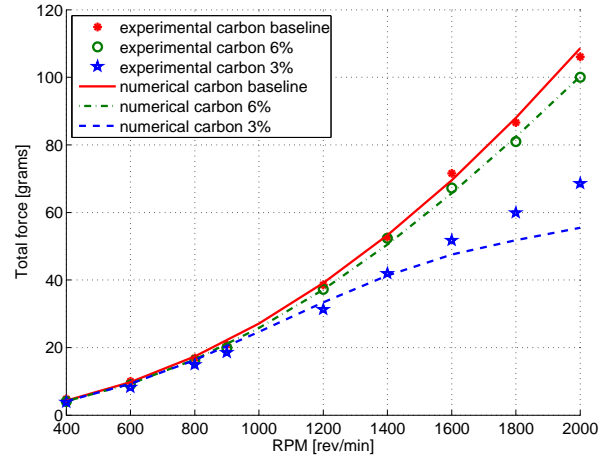
(b) Blade pitching amplitude=30°
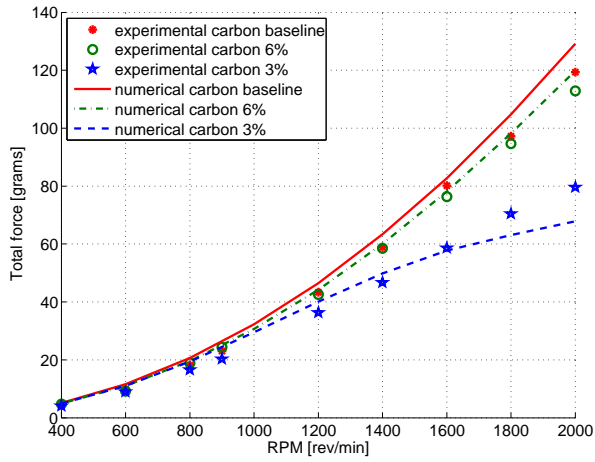
(c) Blade pitching amplitude=35°

(d) Blade pitching amplitude=40°

Figure 19. Comparison of the predicted average total force with experimental data for a 3-bladed rotor using baseline NACA blades and 6% and 3% flat plate blades.

American Institute of Aeronautics and Astronautics

accurately. Therefore, an aeroelastic model based on MBDyn and uniform inflow was used for the flexible blade validations.

Figure 18 shows the vertical and lateral force comparison and Fig. 19 shows the total force comparison of the predictions with experimental results for the baseline NACA 0010 carbon blade, 6% carbon blade and 3% flexible carbon blade. Figure 18(a) compares the vertical force prediction with the experimental measurements for a 3-bladed rotor at 30° pitching amplitude. It can be seen that for the baseline NACA 0010 blade and the 6% carbon blade, the predictions were very accurate. However, for the 3% carbon blade, the model is able to predict the forces accurately at lower rotational speeds, however, there is an underprediction above 1200 rpm. However, the model accurately captures the trend in the variation of vertical force for the 3% blade. Figure 18(b) compares the predicted lateral forces with measured values for the same case. Again, it can be clearly seen that the predictions for the baseline NACA blade and 6% blade are good. However, for the flexible 3% blade, even though the predicted values are close to the experimental values, the lateral force is overpredicted at lower rotational speeds, and underpredicted at higher rotational speeds. The resultant thrust validation for 25°, 30°, 35° and 40° pitching amplitudes for a 3-bladed rotor are shown in Fig. 19. Again, the resultant thrust is predicted accurately for the stiffer blades, however, for the 3% flexible blades there is an underprediction of the thrust at higher rotational speeds.

One reason for the inaccurate prediction of the thrust at higher rotational speeds is the fact that the deformations increase with rotational speed and hence their contribution to the blade aerodynamic loads increases. Therefore the ability to predict deformations accurately and to include their influence in the aerodynamic forces becomes important. The underprediction in thrust may be attributed to the overprediction of deformations at higher speeds or the inaccuracies in including the effect of deformations on aerodynamic loads. However, the overall prediction for the flexible 3% blade is quite satisfactory considering the fact that the blades are undergoing large deformations (blades twist up to 40° at the tip for 2000 rpm (Fig. 14(f))).

Figure 20 shows the variation of geometric angle of attack of the blades $(\theta + \hat{\phi})$ at the mid-span and tip for the baseline NACA 0010 blade and also the flexible 3% blades for a pitching amplitude of 40°. It should be noted that these are geometric angles and therefore do not have the effect of inflow. From Fig. 20(b) it can be clearly see that for the flexible 3% blade the drop in thrust at higher rotational speeds is due to the large nose-down twist in the upper half $(\Psi = 0°–180°)$, which significantly decreases the geometric angle of attack. However, there is a small nose-up twist in the lower half $(\Psi = 180°–360°)$ especially at the tip, however, this is much smaller than the nose-down twist in the upper half and is not sufficient to compensate for the loss of lift in the upper half and this effectively decreases the net force. However, as shown in Fig. 20(a), for the baseline NACA 0010 carbon blades, the twist is significantly small and the geometric angles of attack are not very different from the prescribed pitch angles.
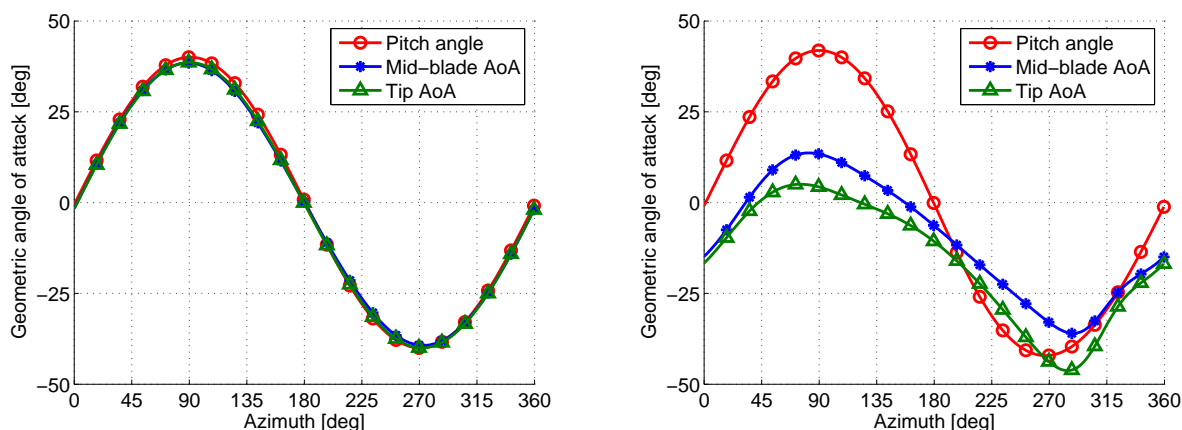
(a) Geometric angle of attack $(\theta + \hat{\phi})$ for the baseline NACA 0010 blade.

(b) Geometric angle of attack $(\theta + \hat{\phi})$ for the 3% flexible carbon blade.

Figure 20. Variation of Geometric angle of attack $(\theta + \hat{\phi})$ at the tip and mid-beam for 40° pitching amplitude.

American Institute of Aeronautics and Astronautics

IV.   SUMMARY AND CONCLUSIONS

The objective of the present work was to develop a refined aeroelastic model that can accurately predict the blade loads and average thrust of a MAV-scale cycloidal rotor. The analysis followed two parallel approaches: (1) non-linear beam finite element analysis with radial bending, tangential bending and torsional degrees of freedom and, (2) multibody based analysis, MBDyn applicable for large deformations. Both the analysis used unsteady aerodynamics assuming attached flow. Two different inflow models, uniform inflow, and double-multiple streamtube (D-MS) were investigated. The analysis was also used to understand the effect of blade flexibility, unsteady aerodynamics and blade kinematics on the cyclorotor performance. The following are specific conclusions drawn from this study:

1. When compared to the experimental measurements, the present analysis was able to predict the magnitude of the resultant thrust vector with sufficient accuracy over a wide range of rotational speeds, pitching amplitudes, number of blades and even for an extremely flexible blade. However, the direction of the resultant thrust vector was not predicted with the same accuracy in all the cases.

2. Even though the multiple streamtube inflow model predicted the instantaneous forces more accurately than the uniform inflow model when compared with the 3-D CFD results, both the inflow models were quite comparable in predicting the average resultant thrust for the baseline NACA 0010 blades.

3. The key reasons for the lateral force production was identified to be the mechanical lag in the actual blade kinematics (easily modeled within the multibody approach) and the aerodynamic phase lag brought about by the unsteady aerodynamics. Another parameter that had a significant influence on the magnitude of the lateral force (with minimal influence on the vertical force) is the drag model used for the blades. Without the contribution from the induced drag, the lateral force was always underpredicted when compared with test data.

4. Even though the deformations were dominated primarily by inertial forces, aerodynamic forces also had significant influence on them. This clearly shows the need for a coupled aeroelastic analysis for predicting the blade loads on a cyclorotor with flexible blades.

5. For the 3% thickness-to-chord ratio flexible blades, the resultant thrust was slightly underpredicted at higher rotational speeds. This may be attributed to the overprediction of structural deformations. Another reason could be the inaccuracies in the accounting for the effect of deformations in blade aerodynamics forces.

6. The key reason for the lower thrust while using flexible blades was identified to be the reduction in geometric pitch angle due to the large nose down torsional deformation of the blades in the upper half of the circular blade trajectory which is not compensated by the nose-up blade deformation in the bottom half as expected. Also, the study showed that a multibody based analysis is required to predict the deformations accurately for very flexible blades.

V.   ACKNOWLEDGEMENT

References

[1]Ifju, P. G., Jenkins, D. A., Ettinger, S., Lian, Y., Shyy, W., and Waszak, M. R., "Flexible-Wing-Based Micro Air Vehicles," Paper AIAA-2002-705, AIAA 40th Aerospace Sciences Meeting and Exhibit, Reno, NV, January 14–17, 2002.

[2]Peterson, B., Erath, B., Henry, K., Lyon, M., Walker, B., Powell, N., Fowkes, K., and Bowman, W. J., "Development of a Micro Air Vehicle for Maximum Endurance and Minimum Size," Paper AIAA-2003-416, AIAA 41st Aerospace Sciences Meeting and Exhibit, Reno, NV, January 6–9, 2003.

[3]Brion, V., Aki, M., and Shkarayev, S., "Numerical Simulation of Low Reynolds Number Flows Around Micro Air Vehicles and Comparison Against Wind Tunnel Data," Paper AIAA-2006-3864, AIAA 24th Applied Aerodynamics Conference Proceedings, San Francisco, CA, June 5–8, 2006.

[4]Grasmeyer, J. M., and Keennon, M. T., "Development of the Black Widow Micro Air Vehicle," Paper AIAA-2001-0127, AIAA 39th Aerospace Sciences Meeting and Exhibit, Reno, NV, January 8–11, 2001.

[5]Keenon, M. T., and Grasmeyer, J. M., "Development of the Black Widow and Microbat MAVs and a Vision of the Future of MAV Design," Paper AIAA-2003-2901, AIAA/ICAS International Air and Space Symposium and Exposition, The Next 100 Years Proceedings, Dayton, OH, July 14–17, 2003.

[6]Pines, D., and Bohorquez, F., "Challenges Facing Future Micro-Air-Vehicle Development," *Journal of Aircraft*, Vol. 43, (2), March/April 2006, pp. 290–305.

[7]Hein, B., and Chopra, I., "Hover Performance of a Micro Air Vehicle: Rotors at Low Reynolds Number," *Journal of American Helicopter Society*, Vol. 52, (3), July 2007, pp. 254–262.

[8]Chopra, I., "Hovering Micro Air Vehicles: Challenges and Opportunities," Proceedings of American Helicopter Society Specialists' Conference, International Forum on Rotorcraft Multidisciplinary Technology, October 15–17, 2007, Seoul, Korea

[9]Benedict, M., Jarugumilli, T., and Chopra, I., "Design and Development of a Hover-Capable Cyclocopter MAV," Proceedings of the 65th Annual National Forum of the American Helicopter Society, Grapevine, TX, May 27–29, 2009.

[10]Sirohi, J., Parsons, E., and Chopra, I., "Hover Performance of a Cycloidal Rotor for a Micro Air Vehicle," *Journal of American Helicopter Society*, Vol. 52, (3), July 2007, pp. 263–279.

[11]Benedict, M., Sirohi, J., and Chopra, I., "Design and Testing of a Cycloidal Rotor MAV," AHS International Specialists' Meeting Proceedings on Unmanned Rotorcraft: Design, Control and Testing, Chandler, AZ, January 23–25, 2007.

[12]Benedict, M., Chopra, I., Ramasamy, M., and Leishman, J. G., "Experimental Investigation of the Cycloidal rotor for a Hovering Micro Air Vehicle," Proceedings of the 64th Annual National Forum of the American Helicopter Society, Montreal, Canada, April 28–30, 2008.

[13]Benedict, M., Chopra, I., Ramasamy, M., and Leishman, J. G., "Experiments on the Optimization of the MAV-Scale Cycloidal Rotor Characteristics Towards Improving Their Aerodynamic Performance," Proceedings of the International Specialists' Meeting on Unmanned Rotorcraft, Scottsdale, AZ, January 20–22, 2009.

[14]Benedict, M., Jarugumilli, T., and Chopra, I., "Experimental Performance Optimization of a MAV-Scale Cycloidal Rotor," Proceedings of the AHS Specialists' Meeting on Aeromechanics, San Francisco, CA, Jan 20–22, 2010.

[15]Yun, C. Y., Park, I. K., Lee, H. Y., Jung, J. S., Hwang, I. S., and Kim, S. J., "Design of a New Unmanned Aerial Vehicle Cyclocopter," *Journal of American Helicopter Society*, Vol. 52, (1), January 2007, pp. 24–35.

[16]Hwang, I. S., Hwang, C. P., Min, S. Y., Jeong, I. O., Lee, C. H., Lee., Y. H., and Kim, S. J., "Design and Testing of VTOL UAV Cyclocopter with 4 Rotors," American Helicopter Society 62nd Annual Forum Proceedings, Phoenix, AZ, April 29–May 1, 2006.

[17]Hwang, I. S., Hwang, C. S., and Kim, S. J., "Structural Design of Cyclocopter Blade System," Paper AIAA-2005-2020, 46th AIAA/ASME/ASCE/AHS/ASC Structures, Structural Dynamics and Materials Conference Proceedings, Austin, TX, April 18–21, 2005.

[18]Kim, S. J., Hwang, I. S., Lee, H. Y., and Jung, J. S., "Design and Development of Unmanned VTOL Cyclocopter," Symposium on Aerospace Science and Technology Proceedings, NC, August 12–14, 2004.

[19]Wheatley, J. B., and Windler, R., "Wind-Tunnel Tests of a Cyclogiro Rotor," NACA Technical Note No. 528, May 1935.

[20]Wheatley, J., "Simplified Aerodynamic Analysis of the Cyclogiro Rotating-Wing System," Technical Report 467, National Advisory Committee for Aeronautics, August 1933.

[21]Kirsten, F. K., "Cycloidal Propulsion Applied to Aircraft," *Transactions of the American Society of Mechanical Engineers*, Vol. 50, (12), 1928, pp 25–47.

[22]Boschma, J. H., "Modern Aviation Applications for Cycloidal Propulsion," Paper AIAA-2001-5267, AIAA Aircraft, Technology Integration, and Operations Forum Proceedings, Los Angeles, CA, October 16–18, 2001.

[23]Gibbens, R., "Improvements in Airship Control using Vertical Axis Propellers," Paper AIAA-2003-6853, 3rd AIAA Annual Aviation Technology, Integration, and Operations (ATIO) Forum Proceedings, Denver, CO, Nov. 17–19, 2003.

[24]Gibbens, R., Boschma, J., and Sullivan, C., "Construction and Testing of a New Aircraft Cycloidal Propeller," Paper AIAA-1999-3906, AIAA 13th Lighter-Than-Air Systems Technology Conference Proceedings, Norfolk, VA, June 28–July 1, 1999.

[25]McNabb, M., "Development of a Cycloidal Propulsion Computer Model and Comparison with Experiment," M.S. Thesis, Department of Aerospace Engineering, Mississippi State University, December 2001.

[26]Nagler, B., "Improvements in Flying Machines Employing Rotating Wing Systems," United Kingdom Patent No. 280,849, issued November 1926.

[27]Iosilevskii, G., and Levy, Y., "Experimental and Numerical Study of Cyclogiro Aerodynamics," *AIAA Journal*, Vol. 44, (12), 2006, pp 2866–2870.

[28]Higashi, Y., Tanaka, K., Emaru, T., and Wang, H. O., "Development of a Cyclogyro-based Flying Robot with Variable Attack Angle Mechanisms," IEEE/RSJ International Conference Proceedings on Intelligent Robots and Systems, Beijing, China, October 9–15, 2006.

[29]Yu, H., Bin, L. K., and Rong, H. W., "The Research on the Performance of Cyclogyro," Paper AIAA-2006-7704, AIAA 6th Aviation Technology, Integration and Operations Conference Proceedings, Wichita, KS, September 25–27, 2006.

[30]Masarati, P., Lanz, M., and Mantegazza, P., "Multistep Integration of Ordinary, Stiff and Differential-Algebraic Problems for Multibody Dynamics Applications," *XVI Congresso Nazionale AIDAA*, Palermo, 24–28 September 2001, pp. 71.1–10.

[31]Hodges, D. H., and Dowell, E. H., "Nonlinear Equations of Motion for the Elastic Bending and Torsion of Twisted Nonuniform Rotor Blades," NASA TN D-7818.

[32]Yang, K., Lakshminarayan, V. K., and Baeder, J. D., "Simulation of a Cycloidal Rotor System Using an Overset RANS Solver," To be presented at American Helicopter Society 66th Annual Forum Proceedings, Phoenix, AZ, May 11–13, 2010.

[33]Migliore, P. G., Wolfe, W. P., and Fanuccif, J. B., "Flow Curvature Effects on Darrieus Turbine Blade Aerodynamics," *Journal of Energy*, Vol. 4, (2), 1980, pp. 49–55.

[34]Lindenburg, C., "BLADMODE Program for Rotor Blade Mode Analysis," Ecn c02-050, 2003

American Institute of Aeronautics and Astronautics

[35]Ghiringhelli, G. L., Masarati, P., and Mantegazza, P., "A Multi-Body Implementation of Finite Volume Beams," Vol. 38, No. 1, January 2000, pp. 131–138, doi:10.2514/2.933.

[36]Leishman, J. G., *Principles of Helicopter Aerodynamics*, Cambridge University Press, Cambridge, UK, 2000.

[37]Bielawa, R. L., *Rotary Wing Structural Dynamics and Aeroelasticity*, AIAA, Washington, DC, 1992.